Context-Dependent PSIICOS: A Novel Framework for Functional Connectivity Estimation Accounting for Task-Related Power Leakage

Daria Kleeva [1] **, Alexei Ossadtchi**[*,1,2,3]

1 Center for Bioelectric Interfaces, Higher School of Economics, Moscow, Russia
[2] AIRI, Artificial Intelligence Research Institute, Moscow, Russia
[3] LLC "Life Improvement by Future Technologies Center"
∗ the corresponding author, ossadtchi@gmail.com

Abstract.

Functional connectivity (FC) analysis using non-invasive neuroimaging methods, such as MEG and EEG, is often confounded by artifacts from spatial leakage and task-related power modulations. To address these limitations, we present Context-Dependent PSIICOS (CD-PSIICOS), a novel framework that improves the estimation of FC by incorporating task-specific cortical power distributions into the projection operator applied to the vectorized sensor-space cross-spectrum. Unlike the original PSIICOS approach, which is prone to suppress spatial leakage from all the sources, CD-PSIICOS dynamically adjusts the projection based on the active source distribution, enabling more accurate suppression of spatial leakage while preserving true zero-phase interactions. We validated CD-PSIICOS using realistic simulations and a multi-subject MEG dataset. The results demonstrate that CD-PSIICOS outperforms the original PSIICOS in suppressing artifacts at lower projection ranks, maintaining robust detection of functional networks across theta, alpha, beta, and gamma frequency bands. By requiring lower projection ranks for optimal performance, CD-PSIICOS facilitates the reconstruction of physiologically relevant networks with improved specificity and stability.

Keywords: functional connectivity, MEG, EEG, spatial leakage, phase synchrony, volume conduction

1. Introduction

Existing evidence strongly indicates that healthy brain functioning and its dynamical properties rely on connectivity between cell assemblies at various resolution levels, which reflects communication between different brain areas (Greicius, 2008). The task of mapping the human connectome remains one of the most significant challenges in neuroimaging (Bassett and Bullmore, 2009), limiting our understanding of the fundamental principles underlying brain function.

Noninvasive time-resolved neuroimaging techniques such as EEG and MEG, combined with source localization methods, offer the potential to examine large scale

functional connectivity (FC) in terms of space, time, frequency, and phase-lag (Ossadtchi et al., 2018). These unique benefits arise from measuring the brain's electrical activity with sensor arrays covering the entire head. To effectively quantify frequency-specific phase coupling, it is essential to employ such measures as cross-spectrum, coherence and their derivatives such as PLV, PLI and others (Bastos and Schoffelen, 2016; Nolte et al., 2004, 2008; Stam et al., 2007), which facilitates the detection of consistent phase relationships over time. Based on the "communication through coherence" principle (Fries, 2015) tracking the dynamics of phase synchrony between the activity of neuronal assemblies allows for exploring the dynamic processes of inter-regional communications implemented by the brain.

However, such FC measures computed from the non-invasively measured electromagnetic signals are prone to Type I and Type II errors. Firstly, the artifacts of volume conduction, or spatial leakage (SL) in MEG, often result in spurious connections between brain regions that do not reflect true neuronal interactions. This problem was addressed with various methods. The most potent approach that gave rise to a family of methods for tracking phase synchrony is based on exploring the imaginary part of the sensor-space coherence (Nolte et al., 2004). The imaginary part of coherence is devoid of the volume conduction contributions due to the instantaneous nature of the latter (Hamalainen et al., 1993) which furnishes certain control over the false positives in the non-invasive FC studies. However, the methods relying on the imaginary part of coherence struggle to detect the networks whose nodes exhibits zero or close to zero mutual phase-lags Ossadtchi et al. (2018) and are therefore prone to generating the false negatives. Ironically, such instantaneous coupling scenarios are ubiquitous which has been shown both theoretically Chawla et al. (2001); Rajagovindan and Ding (2008); Fischer et al. (2006); Vicente et al. (2008); Esfahani and Valizadeh (2014); Gollo et al. (2014) and empirically (Gray et al., 1989; Frien et al., 1994; Roelfsema et al., 1997; Rodriguez et al., 1999; Fell et al., 2001; Havenith et al., 2009; König et al., 1995) in numerous studies.

In (Ossadtchi et al., 2018; Altukhov et al., 2023) we introduced PSIICOS (Phase shift invariant imaging of coherent sources) approach, which, by operating on the vectorized $\mathrm{M} \times \mathrm{M}$ sensor-space cross-spectrum, effectively suppresses the spatial leakage and without completely removing the genuine true zero-phase coupling.

PSIICOS uses a specifically designed projection operation that yields significant suppression of the volume conduction effect in the real part of the cross-spectrum while retaining the contributions modulated by the off-diagonal elements of the source-space cross-spectral matrix. However, due to the fundamental reasons it is impossible to completely zero the spatial leakage contributions and overly powerful task-related induced activity generated by the genuinely uncoupled cortical sources may still lead to the false positives (Schoffelen and Gross, 2009; Bastos and Schoffelen, 2016; Kleeva and Ossadtchi, 2021). In these cases the power and selectivity of PSIICOS projection may appear insufficient due to its universality as it is designed to suppress the field spread contributions and the associated mutual spatial leakage from *all* cortical sources

(Altukhov et al., 2023).

In this paper we extend the original PSIICOS technique by constructing the projection operator that takes into account the distribution of active sources pertinent to the analyzed data. Instead of building the projection operator using the $M^2 \times 1$ auto 2-topographies of *all* sources present in the forward model matrix here we propose to take into account the cortical power distribution context.

After describing the methodological aspects of the context dependent PSIICOS (CD-PSIICOS) technique we first validate this framework through testing using the realistically simulated data. We show its superior performance as compared to the generic PSIICOS and explore the extent to which the CD-PSIICOS depends on the particular inverse operator used to obtain the distribution of the induced cortical activity power. We also show that CD-PSIICOS requires lower optimal projection rank as compared to the original PSIICOS which means that potentially more of the genuine close to zero-phase networks will be retained after the projection.

Then, we demonstrate the application of CD-PSIICOS to real data using a multi-subject 275-channel CTF MEG dataset recorded from nine volunteers during an audio-motor integration task.

We explore the stability of the observed networks and the extent to which they are affected by the variation of the PSIICOS projection rank. We report the spatial and the temporal profiles of the discovered networks in the alpha, beta, theta and gamma bands and assess their physiological validity given the behavioral paradigm used to collect the data.

We also verify that the discovered networks indeed correspond to the induced activity with random absolute phase and the persistent phase difference that appeared to be close to zero for the networks derived from the CD-PSIICOS de-biased real part of the cross-spectrum. We also make similar observation but for the more conventional networks manifested in the imaginary part of the cross-spectrum with the peak of the phase difference distribution at $\phi = \pi/2$.

2. Methods

2.1. Generative model

The EEG/MEG setup captures electrophysiological data through an M-channel device that senses the activity neuronal sources distributed over the cortical surface. This surface is digitized into a mesh with N vertices to comprise the source space according to the brain's anatomical features. Each vertex in the mesh is linked to a neuronal source that is approximated by an equivalent current dipole (ECD). Data from K trials is produced by mapping ECD activity to sensor measurements, which mixes the activity from different sources on each sensor and contaminates the mixture the additive measurement noise. Taking into consideration only induced activity, typically analyzed in the time-frequency domain, we can describe the observed data at a given time t,

frequency f within a trial k with the following generative equation:

$$\mathbf{x}^k(f,t) = \sum_{i=1}^{N} \mathbf{g}_i s_i^k(f,t) + \mathbf{n}^k(f,t), \tag{1}$$

where $\mathbf{g}_i$ represents the topography of the i-th source, i-th column of forward operator $\mathbf{G}$, s_i^k represents $i-$th source activity at trial k and $\mathbf{n}^k(f,t)$ models zero mean additive sensor noise.

Based on the theory introduced in (Ossadtchi et al., 2018; Altukhov et al., 2023), the task of FC estimation can be performed in one step without separate reconstruction of source activations $s_i^k(f,t)$.

To show this we first substitute (1) in the definition of sensor-space cross-spectrum $\mathbf{C}^{xx}(f,t) = E\{\mathbf{x}(f,t)\mathbf{x}^H(f,t)\}$ to obtain the vectorized form $\mathbf{C}^{xx}(f,t)$ as

$$vec(\mathbf{C}^{xx})(f,t) = \sum_{i=1}^{N} \mathbf{q}_{ii} c_{ii}^{ss}(f,t) + \sum_{\substack{i,j=1 \\ i\neq j}}^{N} \mathbf{q}_{ij} c_{ij}^{ss}(f,t) + vec(\mathbf{C}^{NN})(f,t), \tag{2}$$

where $\mathbf{q}_{ij} = \{\mathbf{g}_i \otimes \mathbf{g}_j + \mathbf{g}_j \otimes \mathbf{g}_i\}$ for the real part of cross-spectrum and $\mathbf{q}_{ij} = \{\mathbf{g}_i \otimes \mathbf{g}_j - \mathbf{g}_j \otimes \mathbf{g}_i\}$ for the imaginary part, $i,j = 1,\dots N, i \leq j$ correspond to 2-topographies computed using the columns $\mathbf{g}_i$ and $\mathbf{g}_j$ of the traditional forward model matrix $\mathbf{G}$.

2.2. Source space cross-spectrum estimation

As demonstrated in (Altukhov et al., 2023) given a set of vectorized symmetric auto 2-topographies

$$\mathbf{\Gamma} = (\mathbf{g}_1 \otimes \mathbf{g}_1, \dots, \mathbf{g}_N \otimes \mathbf{g}_N) \tag{3}$$

and the orthogonal projector $\mathbf{P} = \mathbf{I} - \mathbf{\Gamma}\mathbf{\Gamma}^\dagger$, vector

$$\mathbf{v}_{ij} = \frac{\mathbf{P}\mathbf{q}_{ij}}{\|\mathbf{P}\mathbf{q}_{ij}\|^2} = \frac{\mathbf{P}\mathbf{q}_{ij}}{\mathbf{q}_{ij}^\top \mathbf{P}\mathbf{q}_{ij}} \tag{4}$$

is the optimal filter that minimizes the cross-talk originating from the mutual spatial leakage when applied to the vectorized cross-spectral matrix (2) as

$$\hat{c}_{ij}^{ss}(f,t) = \mathbf{v}_{ij}^\top vec(\mathbf{C}^{xx})(f,t) \tag{5}$$

Within the CD-PSIICOS approach, we propose modifying the filtering process to account for the active sources present in the data, namely the component $c_{ii}^{ss}(f,t)$ from Eq. 2. This can be achieved by weighting each column i of $\mathbf{\Gamma}$ by estimated power of the i-th source as detailed next.

2.3. The general CD-PSIICOS pipeline

The standard processing procedure involves bandpass filtering the epoched data within the frequency band of interest. After filtering, we compute the outer products of the Hilbert transforms of this data for each epoch. By averaging these outer products across epochs, we obtain the time-varying sensor-space cross-spectral coefficients, denoted as $\mathbf{C}^{xx}(f,t)$. Finally, we estimate the averaged band-specific power distribution across the cortex using one of the standard linear inverse operators, $\mathbf{W}$:

$$\mathbf{p} = \{p_i\} = diag(\mathbf{W}\overline{\mathbf{C}^{xx}(f,t)}\mathbf{W}^\top), \tag{6}$$

where the bar over the sensor-space cross-spectral matrix $\mathbf{C}^{xx}(f,t)$ denotes its mean value computed over specific frequency and time range of interest.

Next, we construct the CD-PSIICOS projection matrix, $\mathbf{P}^{CD}$ by performing a singular value decomposition (SVD) on the modified matrix $\mathbf{\Gamma}^{CD}$ constructed similarly to the original PSIICOS $\mathbf{\Gamma}$, see (3), but using auto 2-topographies scaled with the corresponding power estimate:

$$\mathbf{\Gamma}^{CD} = (\tilde{p}_1\mathbf{g}_1 \otimes \mathbf{g}_1, \ldots, \tilde{p}_N\mathbf{g}_N \otimes \mathbf{g}_N), \tag{7}$$

where $\tilde{p}_i = p_i/\|\mathbf{p}\|$ is the normalized frequency band and time interval specific power of the i-th source, $i = 1, \ldots, N$. The $\mathbf{P}^{CD}$ is then computed as

$$\mathbf{P}^{CD} = \mathbf{I} - \mathbf{U}_R\mathbf{U}_R^\top, \tag{8}$$

where $\mathbf{U_R}$ is the matrix of the first R left singular vectors of the power distribution context dependent $\mathbf{\Gamma}^{CD}$ defined above.

Originally, the only adjustable parameter of the projection was the rank R, which is selected based on the optimal trade-off between the suppression of the SL subspace and the preservation of the real part of the cross-spectrum subspaces. In this study, we specifically examined how the CD-PSIICOS projection behaves at different ranks in comparison to the original projection. Furthermore, since the CD-PSIICOS projector is influenced by the choice of the inverse operator, its regularization parameters, and weighting techniques, we also investigated the robustness of the observed solutions with respect to these parameters.

2.4. Realistic simulations

To evaluate the proposed approaches, we conducted a series of realistic simulations similar to those used in the original paper (Ossadtchi et al., 2018). We utilized a cortical surface model containing 15 000 vertices and a high-resolution forward-model matrix. Each pair of columns in this matrix represented two orthogonally oriented dipoles in the two-dimensional space orthogonal to the right singular vector associated with the smallest singular value of the original forward matrix.

The dataset included 100 epochs. To model the induced activity of coupled sources, we used two 10 Hz harmonics with random phases at the start of each epoch. Phase jitter was drawn from a random distribution within the range of $[-\pi/2, \pi/2]$, with a mean phase lag of $\phi = \pi/20$. In our study, we simulated two truly coupled networks and one network characterized by a lack of coupling (phase jitter assigned as 2π) and excess power (source activation for the network scaled by a factor of 3). This excess power was expected to result in high cross-spectrum values and overestimation of FC.

Brain noise was modeled as the sum of narrow-band signals drawn from a Gaussian distribution. These bands were filtered using a 5th-order band-pass IIR filter, corresponding to the theta (4-7 Hz), alpha (8-12 Hz), beta (15-30 Hz), and gamma (30-50 Hz, 50-70 Hz) frequency ranges. The signal-to-noise ratio was defined as the ratio of the Frobenius norms of the induced and brain noise time series filtered in the band of interest (8-12 Hz). The power spectral density matched the spectral characteristics of EEG or MEG data. Sources were projected into the sensor space through a linear combination of the corresponding columns of the forward matrix.

In practical scenarios, source coordinates do not align with a vertex in the mesh. Therefore, prior to estimating the sensor-space cross-spectrum and constructing the PSIICOS projector, we used a 10-fold sparser cortical model with 1503 nodes.

The power of the sources incorporated to the CD-PSIICOS projector was estimated using the standard inverse operators (MNE (Hämäläinen and Ilmoniemi, 1994) and sLORETA (Pascual-Marqui et al., 2002)) $\mathbf{W}$ applied to the original sensor-space cross-spectrum as $\mathbf{W} \times \mathbf{C}^{xx} \times \mathbf{W}^{\top}$ and DICS beamforming approach (Gross et al., 2001), implying application of the separate spatial filter for each dipole. Additionally, we considered condition, where the auto-topographies were weighted with respect to the ground-truth active sources. The weighting coefficient for ground-truth solution was set to 10, the influence of the degree of weighting was examined separately.

Below is presented the spatial profiles of the modeled networks we used for representative example and the clusters of uncoupled active sources (see Fig. 1, A). The temporal profiles of the coupling were set up in such a way that their activity partially overlapped (see Fig. 1, B).

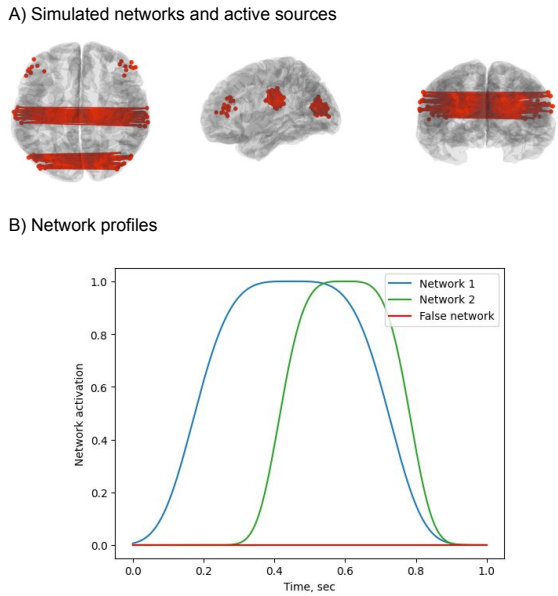

Figure 1: Modeled networks (A) and their activations (B) for representative example

To evaluate the accuracy of proposed approaches we used Receiver Operating Characteristics (ROC) curves. Sensitivity and specificity are defined as follows:

$$\text{sensitivity} = \frac{TP}{TP + FN}$$
$$\text{specificity} = \frac{TN}{FP + TN},$$

where TP, FN, FP and TN are the numbers of true positives, false negatives, false positives and true negatives correspondingly.

In our simulations, each truly coupled network corresponded to a pair of nodes in the high-resolution cortical mesh. For estimating source-space cross-spectral coefficients, we used a sparser cortical mesh. A pair of sources was considered a true connection if their coordinates fell within a specified neighborhood of the original coordinates.

It is important to note that truly coupled sources constitute only a small fraction of all possible connections. Consequently, a high true negative rate was expected. Therefore, for our modifications of original approach to achieve high accuracy, it was essential to attain high specificity values along with a low false alarm rate.

2.5. Real data

We confirmed the suggested method's effectiveness by employing the real MEG data for validation.

The participants were drawn from an open dataset of MEG recordings (Nugent et al., 2022). As stated in the original paper, eligible participants were adults aged

18 or older, in good health, fluent in English, and capable of providing informed consent. The electronic consent for online screening and the written consent for the subsequent recordings were obtained from each of the participants. Exclusion criteria included significant health conditions, substance use, suicidal behavior, abnormal clinical findings, or low educational attainment or cognitive ability.

A total of nine healthy adult individuals (average age: 29.7, 4 males, 5 females) volunteered to take part in the study. MEG data were collected using a a 275 channel CTF MEG system (CTF MEG, Coquiltam BC, Canada). To correct for noise, third-order gradient balancing was employed. Data collection was conducted at a sampling rate of 1200 Hz, with a quarter-Nyquist filter set at 300 Hz.

During the experiment, participants underwent a three-stimulus oddball task that involved presentation of the standard 1000kHz tone, a higher-pitched 1.5kHz target tone and a white noise. Participants were asked to respond to the target tone.

The bandpass-filtered data underwent epoching within a window of -0.2 to 0.8 seconds relative to the stimulus onset, and baseline correction was applied to the segment starting 200 ms before the stimulus onset. Subsequently, sensor-space cross-spectral time series were computed using the averaged outer products of Hilbert-transformed epochs, which then were used within PSIICOS-projection and inverse modeling. The participant's anatomical MRI was used with FreeSurfer software to reconstruct the cortical surface model.

In the context of group analysis, the 'fsaverage' cortical source space was morphed to match each individual's space. Subsequently, following computations performed on the forward models derived from these morphed source spaces, the group solutions were estimated within the 'fsaverage' space.

3. Results

3.1. Realistic simulations

The results based on realistic simulations indicate that CD-PSIICOS approach outperforms the standard one in terms of ROC AUCs, particularly at lower projection ranks (see Fig. 2, A). Specifically, at a fixed projection rank of of 40 (Fig. 2, B), the CD-PSIICOS with MNE-derived weighting demonstrates superior performance compared to both solutions based on sLORETA and the ground truth. The standard PSIICOS and the DICS-based solution lags significantly behind, showcasing reduced sensitivity and specificity at this lower rank. At a projection rank of 80 (Fig. 2, C), the distinction between the CD-PSIICOS variants and the standard PSIICOS approach becomes more nuanced. The overall performance of all CD-PSIICOS approaches converges, while standard PSIICOS shows significant improvement at this rank but still fails to match the accuracy and specificity achieved by the CD-PSIICOS solutions, particularly in the lower FPR range. Finally, at a high projection rank of 200 (Fig. 2, D), the differences between the methods diminish further, with all variants of CD-PSIICOS

and the standard PSIICOS performing comparably.

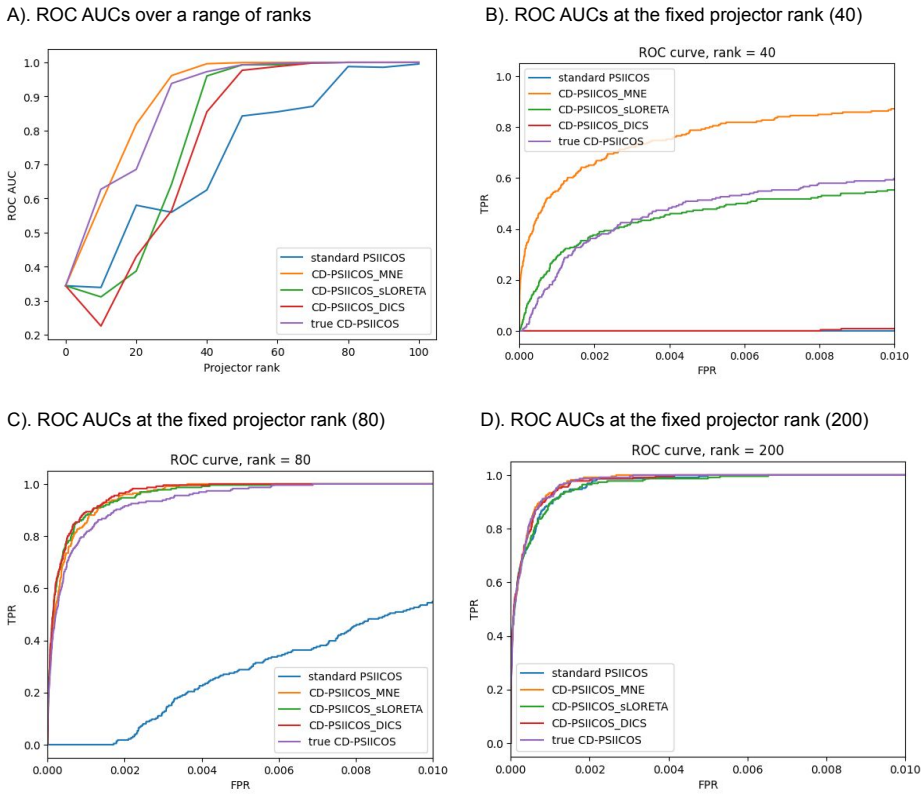

Figure 2: The impact of the standard PSIICOS approach and CD-PSIICOS variations on ROC AUCs across various projector ranks (A) and the detailed comparison of ROC curves at fixed ranks (B-D)

To examine the properties of the obtained solutions using a representative example, we first obtained power profiles on the cortex using various inverse solutions. As evident from Fig. 3 (A-C), the activations of the sources align with the ground truth locations of the uncoupled, exceedingly active sources (Fig. 3 (D)). Notably, sLORETA and DICS solutions exhibit more diffuse patterns compared to the MNE.

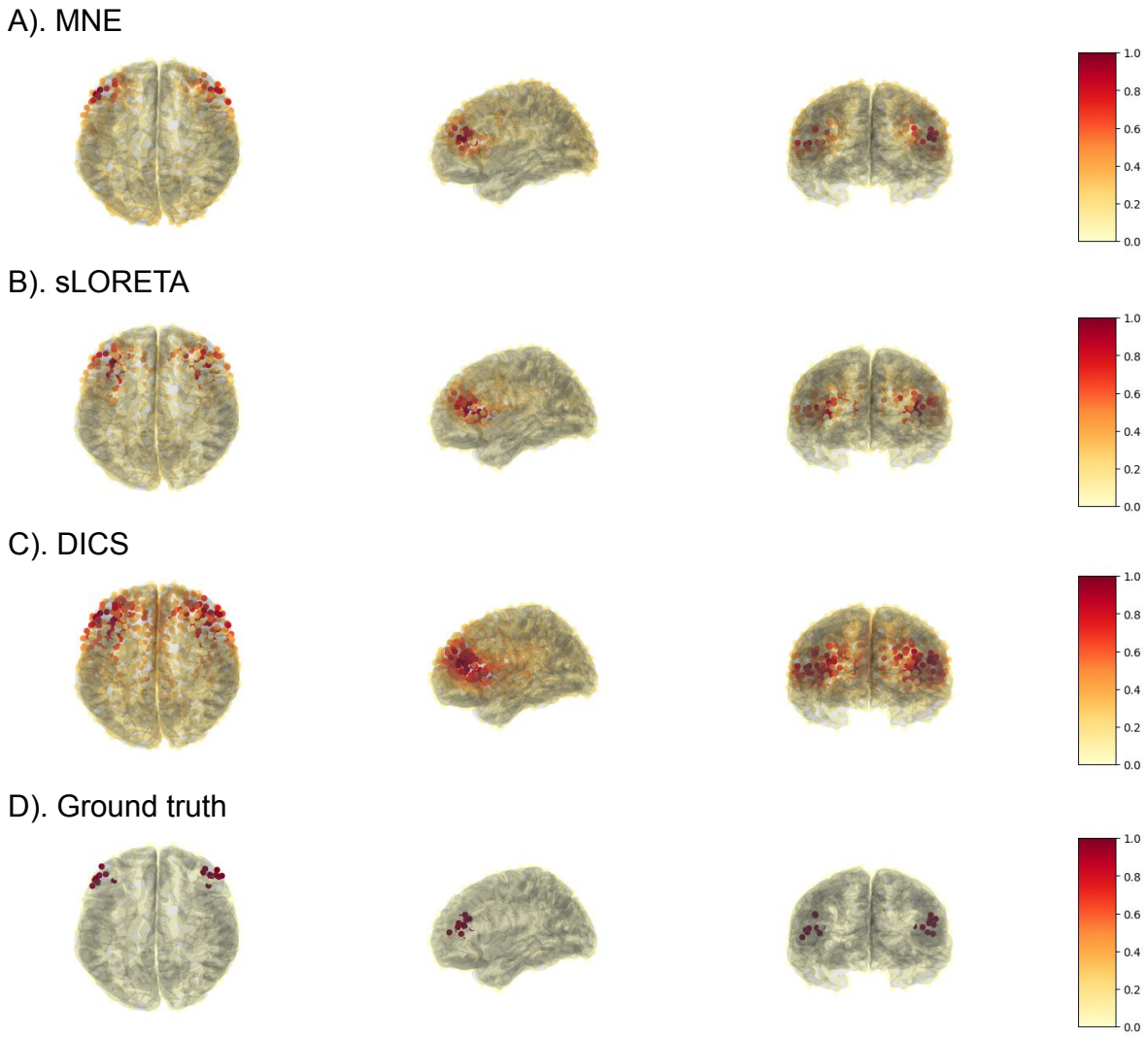

Figure 3: Power profiles obtained after applying inverse operators to the original sensor-space cross-spectrum: (A) MNE, (B) sLORETA, (C) DICS; and ground truth locations of active sources (D)

To evaluate the characteristics of the obtained PSIICOS and CD-PSIICOS projectors, we present the singular value spectra showing the 100 largest singular values obtained for each set of 2-topographies (see Fig. 4). It is evident that the matrix of 2-topographies scaled by the corresponding source power values exhibits a much faster decay of singular values compared to the standard PSIICOS. This indicates that CD-PSIICOS can suppress the volume conduction contribution to the cross-spectrum more efficiently due to focusing on the active sources.

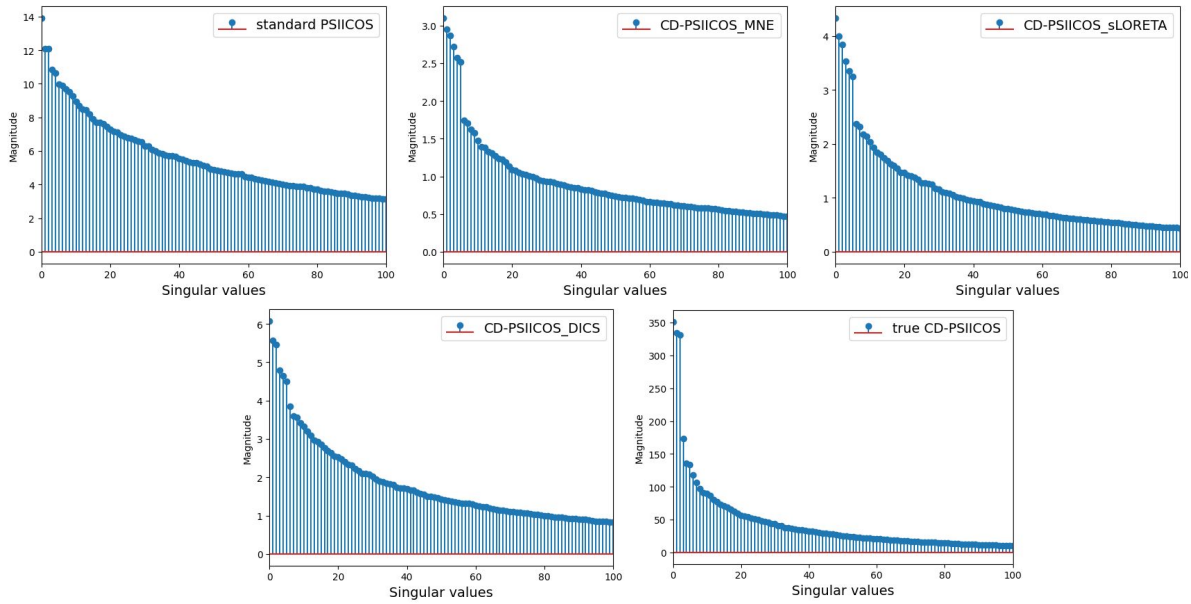

Figure 4: Singular values for each set of 2-topographies: (A) standard approach (A) CD-PSIICOS & MNE, (B) CD-PSIICOS & sLORETA, (C) CD-PSIICOS & DICS; CD-PSIICOS & and ground truth locations of active sources (D)

The subsequent comparison of the standard PSIICOS approach and CD-PSIICOS variations (see Fig. 5) revealed that at low projector ranks (20, 40, 80), the standard PSIICOS was biased towards the clusters of active uncoupled frontal sources. Even at a higher projector rank of 200, while the true networks were reconstructed, residual false clusters from the active sources were still observed. On the other hand, the CD-PSIICOS approach based on the MNE, although showing false pairs due to remaining SL effects at rank=20, began to reconstruct the true networks from rank=40 onwards and was not biased towards the active uncoupled sources. CD-PSIICOS based on sLORETA, DICS, and the ground truth began to show consistent networks at the higher projector ranks.

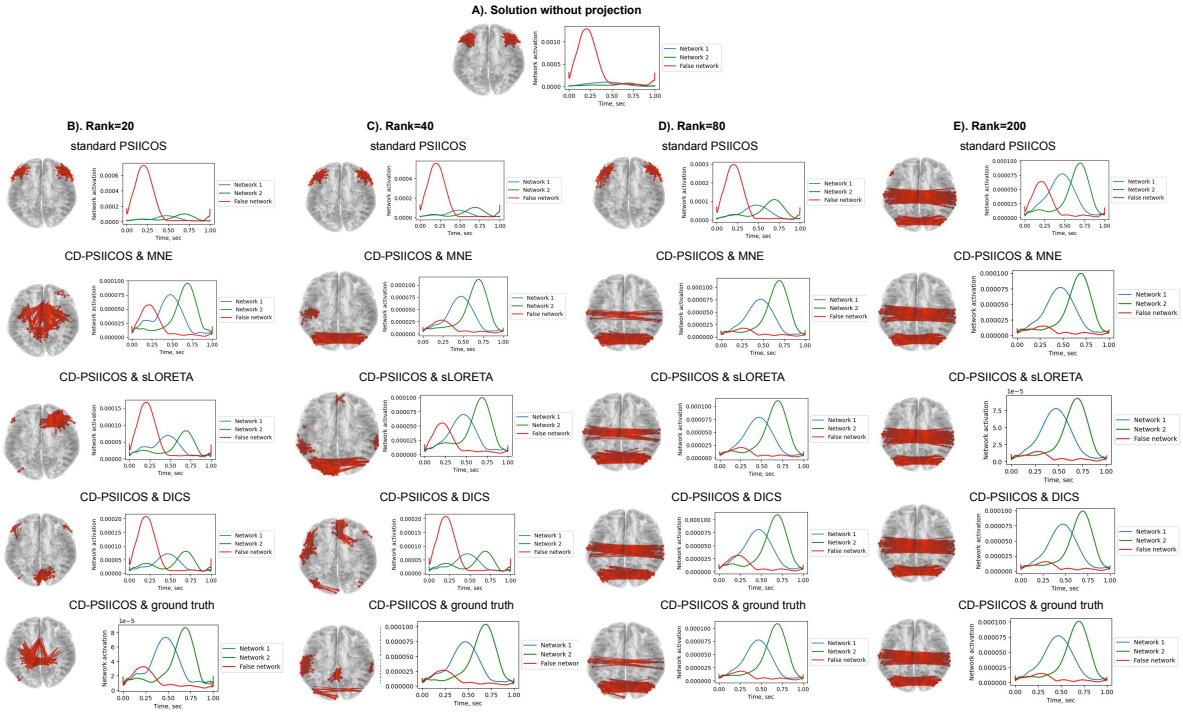

Figure 5: Spatial and temporal activation profiles of the networks reconstructed without PSIICOS approach (A) and with standard PSIICOS and CD-PSIICOS approaches at ranks equal to 20 (B), 40 (C), 80 (D) and 200 (E). The depicted pairs of nodes are derived from top N=300 largest cross-spectral coefficients.

To better understand the performance of CD-PSIICOS compared to standard PSIICOS, we analyzed the norms of the cross-spectral coefficients for two groups: truly coupled networks and falsely coupled (uncoupled) networks (see Fig. 6). These norms represent the strength of connectivity estimated by the method, with higher values indicating stronger interactions. For falsely coupled networks, the CD-PSIICOS solutions showed a much sharper reduction in norm values compared to the standard PSIICOS solution. This indicates that CD-PSIICOS is more effective at suppressing spurious connections caused by spatial leakage, effectively improving the signal-to-noise ratio (SNR) for identifying genuine connectivity. Among the CD-PSIICOS variants, the solutions weighted by MNE and the ground truth exhibited the largest drop in norm values for the uncoupled networks. In contrast, the sLORETA- and DICS-weighted solutions displayed a less pronounced decrease. Importantly, the norm of the cross-spectral coefficients for falsely coupled networks in the CD-PSIICOS solutions fell below that of truly coupled networks, further demonstrating their improved specificity. This explains the improved ROC performance observed for CD-PSIICOS, as the separation between true and false connectivity becomes more pronounced.

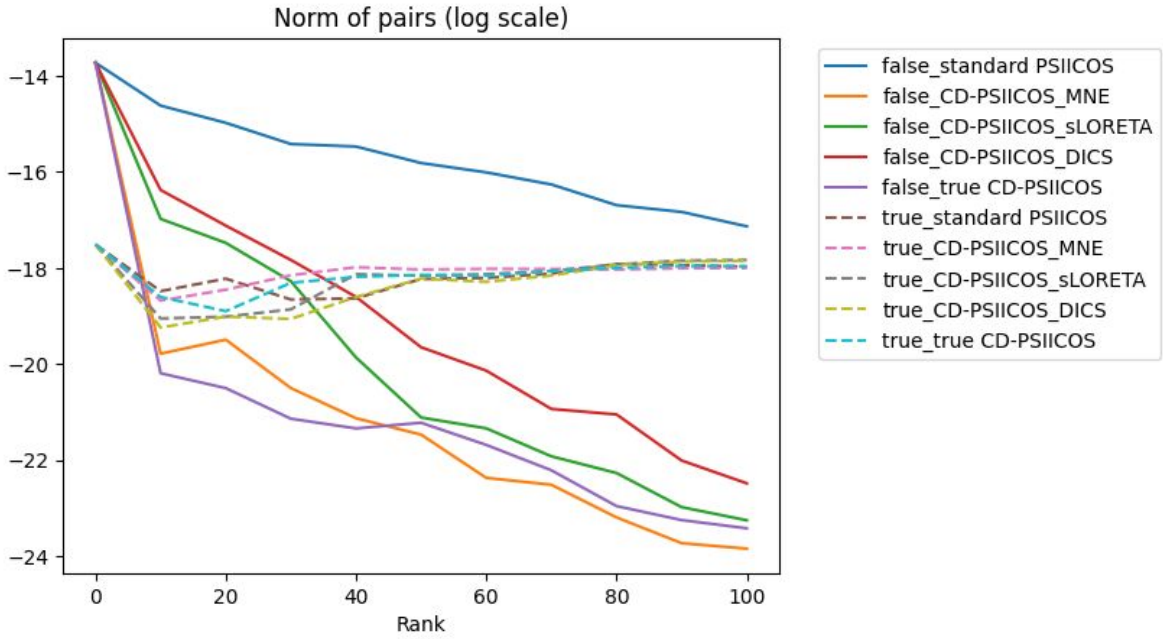

Figure 6: Norms of cross-spectral coefficients in the regions of truly coupled networks and uncoupled pairs depending on the type of solution and projection ranks

To analyze the general characteristics of the proposed modifications, we computed attenuation curves similar to those in (Ossadtchi et al., 2018; Altukhov et al., 2023) that demonstrate the trade-off between suppressing spatial leakage and retaining the information about true interactions within source pairs. Originally, when the curves were computed exclusively using the model, we defined the spatial-leakage subspace and the subspace of the real part of the cross-spectrum using 2-topographies obtained from the forward model. For the current comparison we computed the data-driven attenuation curves and accounted for a thresholded set of active sources with high power estimated through inverse modeling. We computed the norms of the auto-topographies (representing spatial leakage) and the 2-topographies (representing the interactions) for these sources and calculated the differences. The optimal rank is defined as the rank at which the attenuation curve reaches its maximum, representing the point where spatial leakage is sufficiently suppressed without compromising the interactions.

The obtained data-driven attenuation curves (see Fig. 7) reveal that CD-PSIICOS approaches achieve their optimal performance at significantly lower ranks compared to the standard PSIICOS. Specifically, the optimal rank is 500 for standard PSIICOS, 150 for both CD-PSIICOS & MNE and CD-PSIICOS & DICS, and 250 for both CD-PSIICOS & sLORETA and CD-PSIICOS based on ground truth.

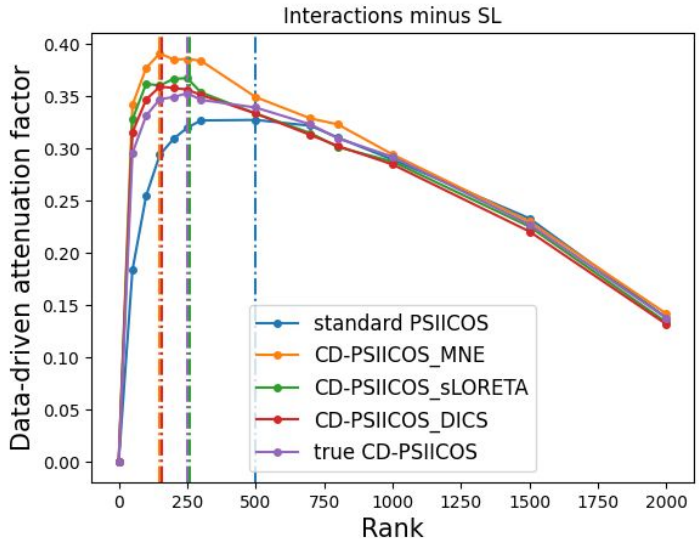

Figure 7: Difference curves between SL components and the real part of cross-spectrum for different solutions and different ranks of projection. The dashed lines represent the optimal projection ranks

Several variable parameters within the proposed approach may potentially affect the algorithm's performance. These parameters include whether thresholding is applied to the coefficients based on the inverse solution used for weighting or if the full inverse solution is utilized, the degree to which the sparse ground-truth-based coefficients are weighted, and the selection of the regularization parameter. Using CD-PSIICOS & MNE at rank=80, we demonstrated that the absence of thresholding or thresholding above 10% of the maximum resulted in higher ROC AUC compared to thresholding at other levels (see Fig. 8 , A). For the CD-PSIICOS solution based on ground truth, we demonstrated that at a fixed rank of 80, the optimal coefficient is 10 (see Fig. 8, B). Finally, the ROC curves based on the CD-PSIICOS solution with MNE demonstrated robustness across a wide range of regularization parameters (see Fig. 8, C). The stability of the solution with respect to the regularization parameter is a critical aspect of the proposed approach, since regularization plays a pivotal role in inverse modeling, as it controls the trade-off between fitting the data and smoothing the solution to avoid overfitting to noise.

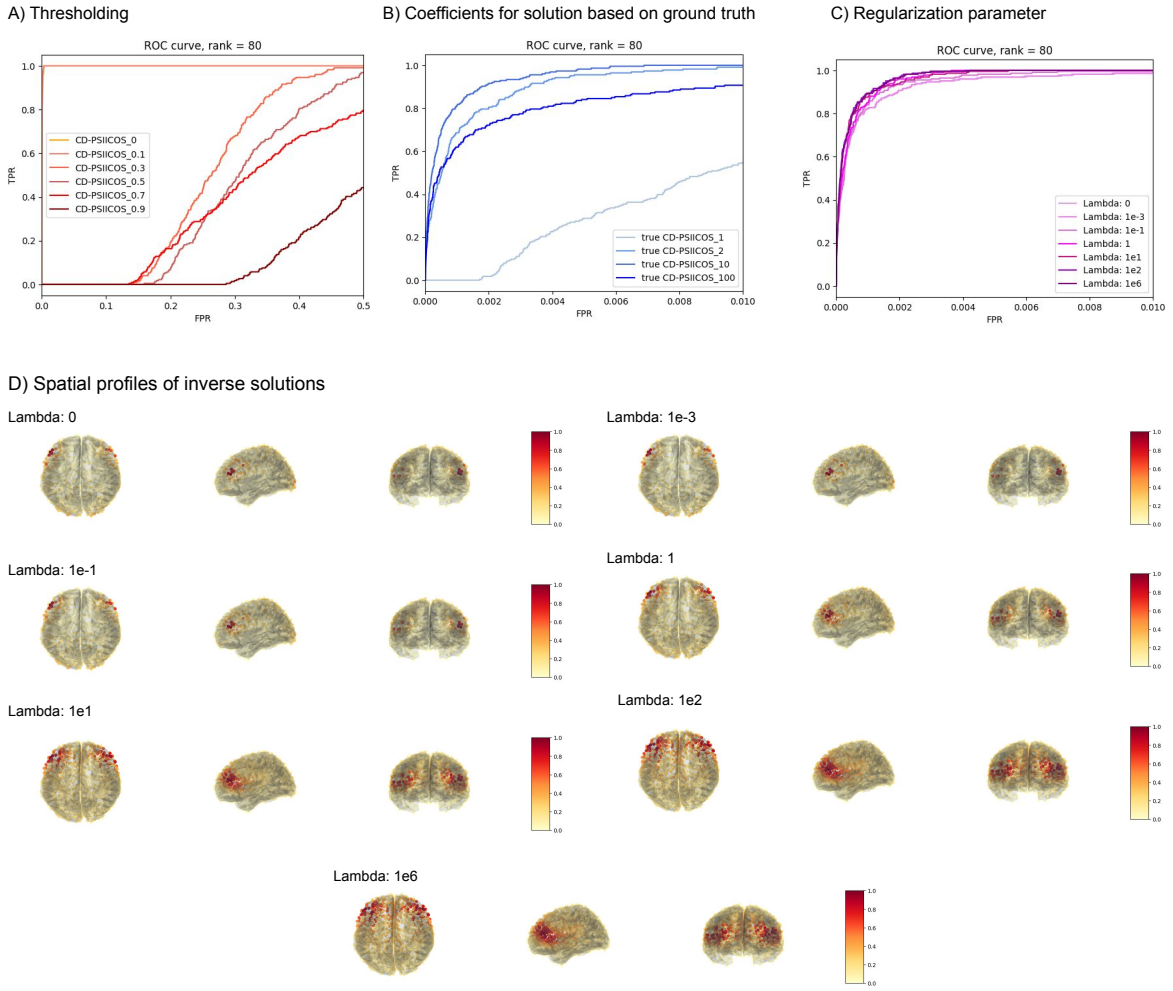

Figure 8: Dependence of performance on (A) thresholding, (B) degree of weighting and (C) regularization parameter with (D) spatial profiles of corresponding inverse solutions

The results from realistic simulations demonstrate that CD-PSIICOS significantly outperforms the standard PSIICOS approach, particularly at lower projection ranks, by effectively suppressing spatial leakage. Among the CD-PSIICOS variants, MNE-based weighting consistently showed superior performance, with optimal projection ranks significantly lower than those required by the standard approach. These findings confirm the robustness and efficiency of CD-PSIICOS in reconstructing functional networks, providing a solid foundation for its application to real MEG data.

3.2. Real data

The grand average of the induced responses and the evoked activity revealed robust differences between the three experimental conditions (see Fig. 9). Specifically, n response to the target tones, we observed induced activity localized to frontal regions in the theta (4–7 Hz) and gamma (30–40 Hz) bands, peaking between 200 and 400 ms after the stimulus onset. Consequently, we focused our initial analysis on these frequency

ranges within the 0–0.5-second time window post-stimulus. Additionally, we analyzed other standard frequency bands, including alpha (8–12 Hz) and beta (13–30 Hz), which showed activity before the stimulus onset. As these bands exhibited desynchronization after the stimulus, we identified active networks in the pre-stimulus window from -0.2 to 0.15 seconds.

Additionally, when visualizing the cross-spectral time series for the active networks in the alpha and beta bands, we normalized their complex cross-spectrum by the square root of the reconstructed power of the sources at each time point.

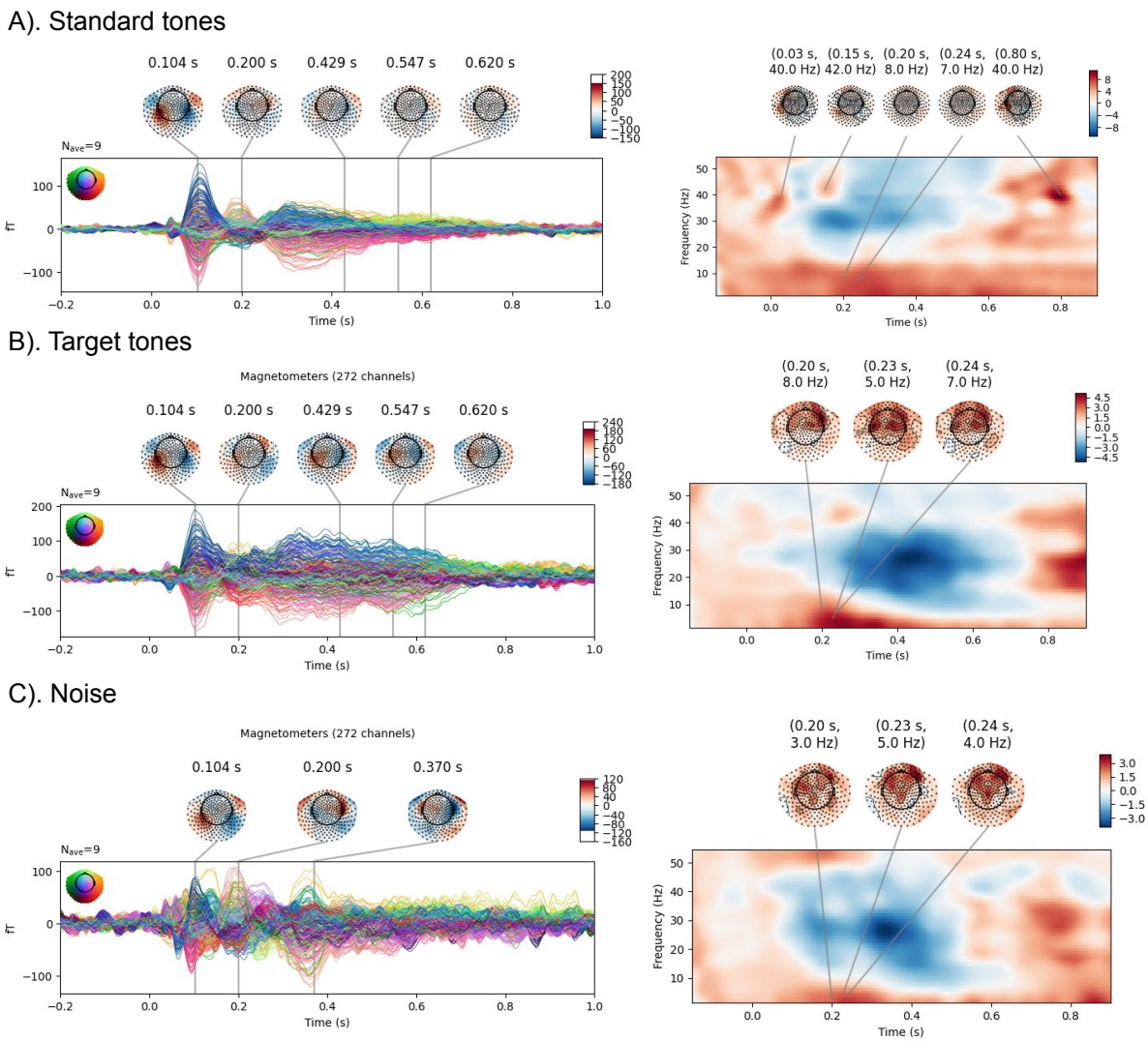

Figure 9: Evoked and induced activity in response to (A) standard tones, (B) target tones and (C) the noise. The color-coded values representing induced activity correspond to z-scores

The MNE-based source localization of the induced activity identified the involvement of the fronto-temporal regions for the theta band(see Fig. 10, A), parietal regions for the alpha band (see Fig. 10, B), somatosensory, motor and frontal regions

for the beta band (see Fig. 10, C) and bilateral frontal regions for the gamma band (see Fig. 10, D). These individual cortical activation maps were subsequently used to construct the CD-PSIICOS projectors.

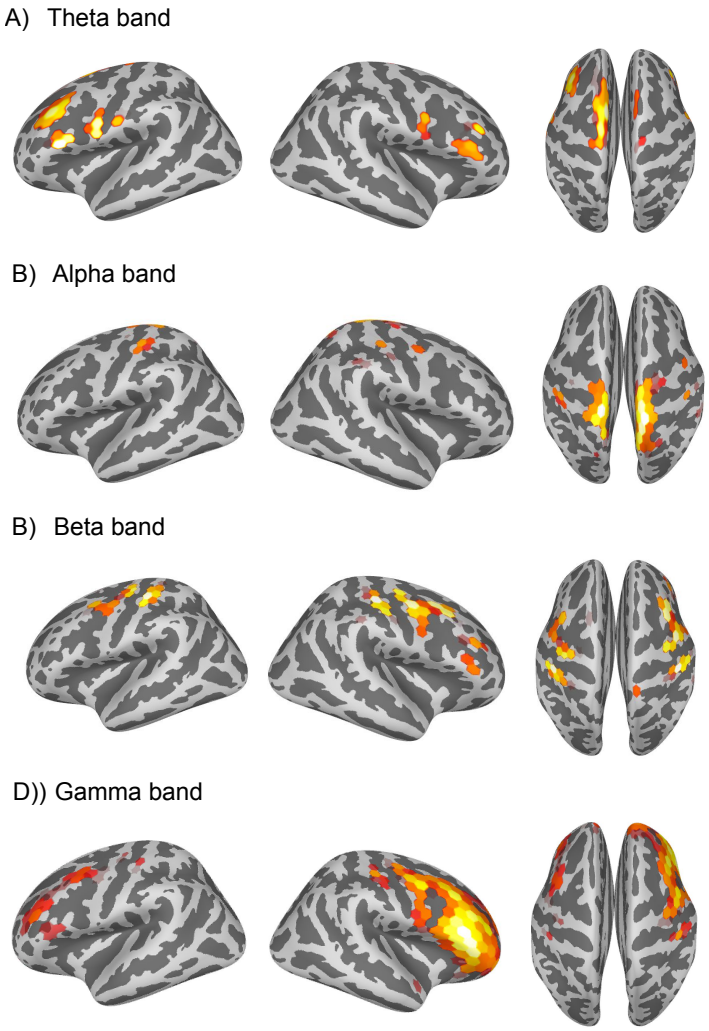

Figure 10: Power profiles of activity in theta (A), alpha (B), beta (C) and gamma (D) bands obtained with MNE inverse operator and used for construction of CD-PSIICOS projectors

The data-driven attenuation curves, illustrating the balance between suppressing the real part of the cross-spectrum and spatial leakage (SL), showed similar patterns to those observed in the simulations (see Fig.7). The optimal rank for the CD-PSIICOS projector was found to be lower than the optimal rank for the standard PSIICOS (see Fig. 11). For the CD-PSIICOS solutions in the theta, alpha and gamma bands, the optimal rank was 30, while in the beta band, it was 50. In contrast, the optimal rank for the standard PSIICOS solutions was equal to 100 across all frequency ranges.

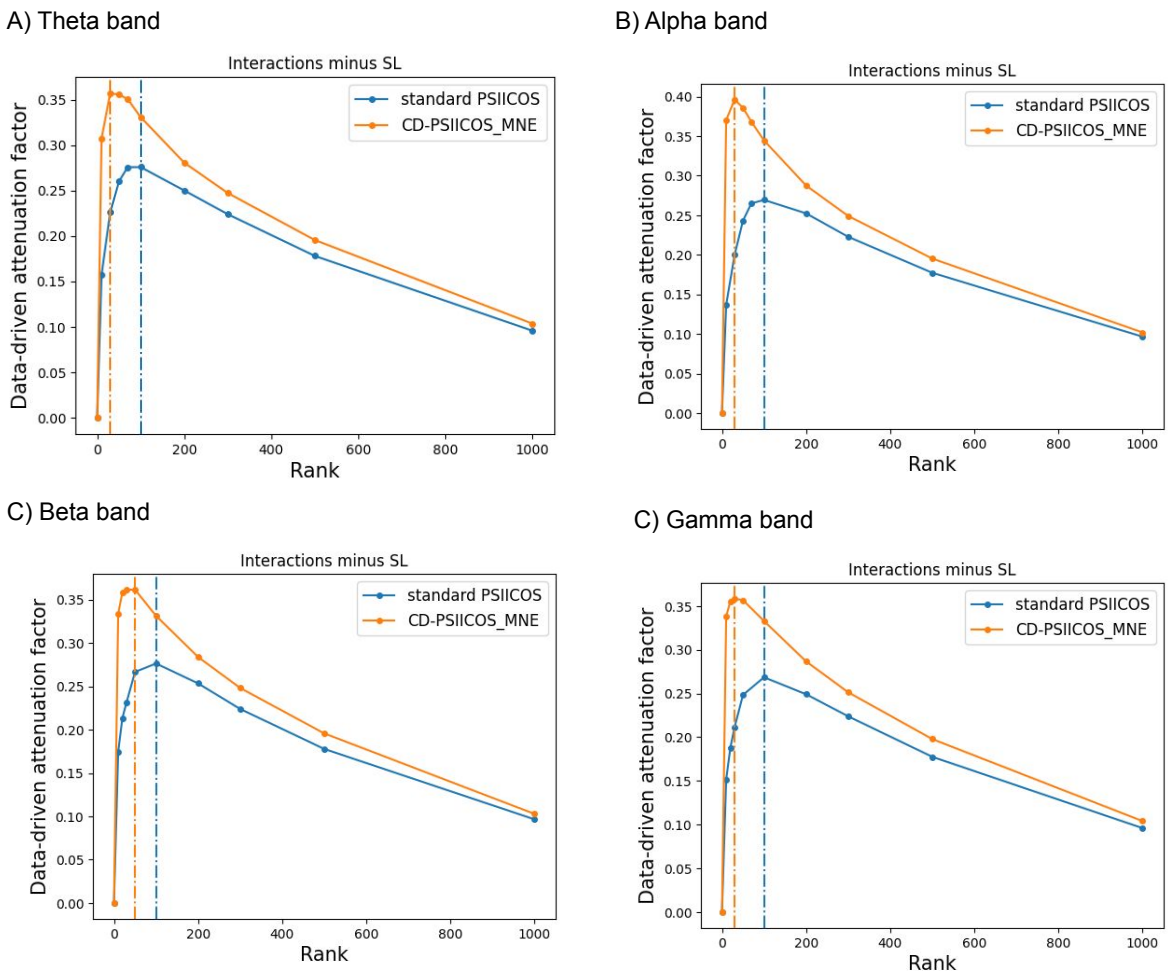

Figure 11: Data-driven attenuation curves for theta (A), alpha (B), beta (C) and gamma (D) bands. The dashed lines represent the optimal projection ranks.

Additionally, we validated that the observed cross-spectral activity indeed corresponded to the coupling with a consistent phase difference profile, irrespective of the absolute phase values. To this end, we identified the latency of the maximal source-space cross-spectral response (obtained based on the real part of projected cross-spectrum). For the $N = 100$ most strongly coupled pairs we extracted the absolute phases and phase differences. Then we created histograms that showed the absolute phases were more uniformly distributed, while the phase differences histograms had peaks around $\phi = 0$ (see Fig. 12). This result indicates the presence of true phase coupling that cannot be explained by the phase-locked activity.

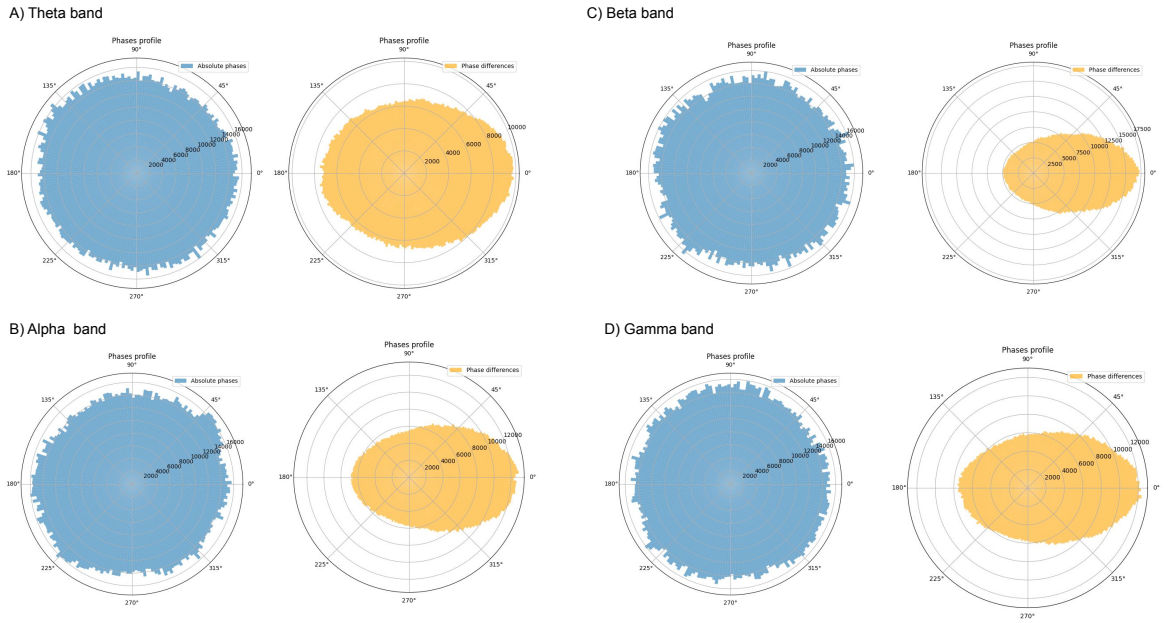

Figure 12: Phase profiles for networks revealed by CD-PSIICOS solution

Finally, we examined the spatial properties of networks and their activation profiles depending on the type of the inverse solution and the projection rank. All the following pictures demonstrate the results of the group analysis over 9 participants.

For the theta band (see Fig. 13), without applying projection, the solution primarily highlights clusters resembling the power distribution of the induced activity. At the projection rank of 10, the standard PSIICOS method shows a partial reduction in spatial leakage but remains biased towards regions with strong power, specifically revealing a distal network with nodes in the left central and right frontal regions. In contrast, the CD-PSIICOS solution at this rank fully suppresses the power-related networks and uncovers a bilateral prefrontal network, characterized by greater spatial symmetry. Additionally, CD-PSIICOS identifies a similar network in the left central and right frontal regions, demonstrating its ability to reconstruct networks comparable to those observed with the standard method. As the projection rank increases to 70, both methods converge on the stable bilateral networks.

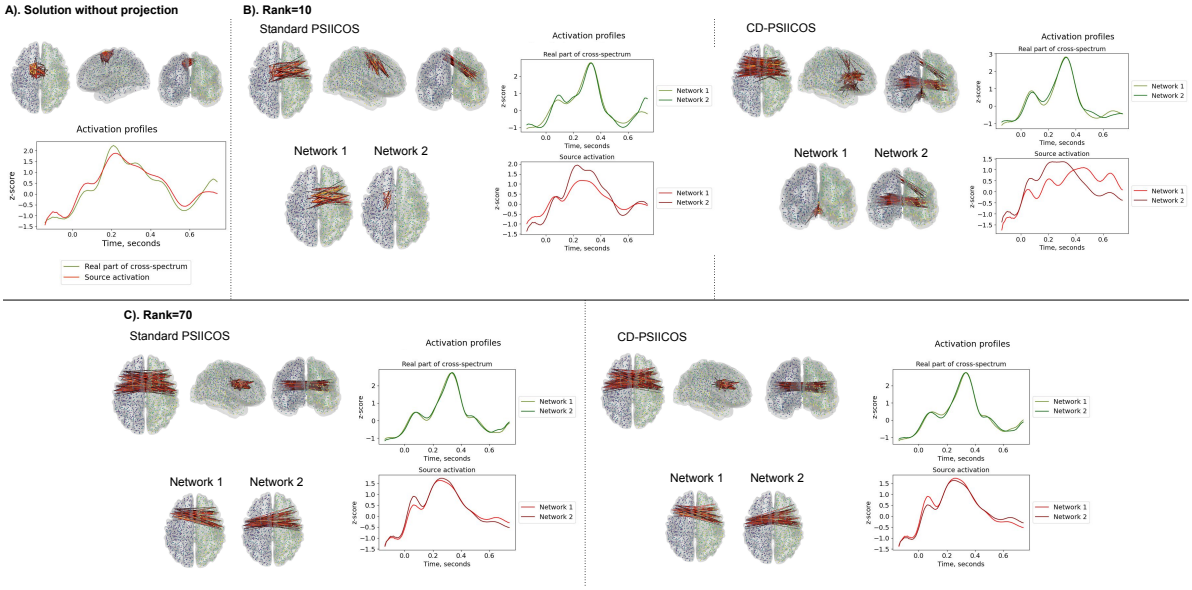

Figure 13: Spatial and activation profiles of the networks in theta band reconstructed without PSIICOS approach (A) and with standard PSIICOS and CD-PSIICOS approaches at ranks equal to 10 (B), and 70 (C)

To further analyze the spatial properties of the networks across projection ranks, we identified networks by clustering the spatial patterns of reconstructed connectivity using the KMeans algorithm. In this analysis, each network was defined as the centroid of a spatial cluster derived from the connectivity patterns reconstructed at each projection rank. This approach allowed us to track the persistence of networks as the projection rank increased.

For the theta band (see Fig. 14), in the standard PSIICOS solution, the relevant network (Network 4, Fig. 14, 1.A) was revealed at higher projection ranks (from the rank of 30). Moreover, at lower ranks, the spatial variability of the networks was more pronounced, suggesting reduced robustness in the reconstruction process. In contrast, the CD-PSIICOS solution revealed the stable network (Network 3, Fig. 14, 2.A) at much lower projection rank of 10. Networks identified by CD-PSIICOS remained consistent in their spatial profiles and locations as the rank increased.

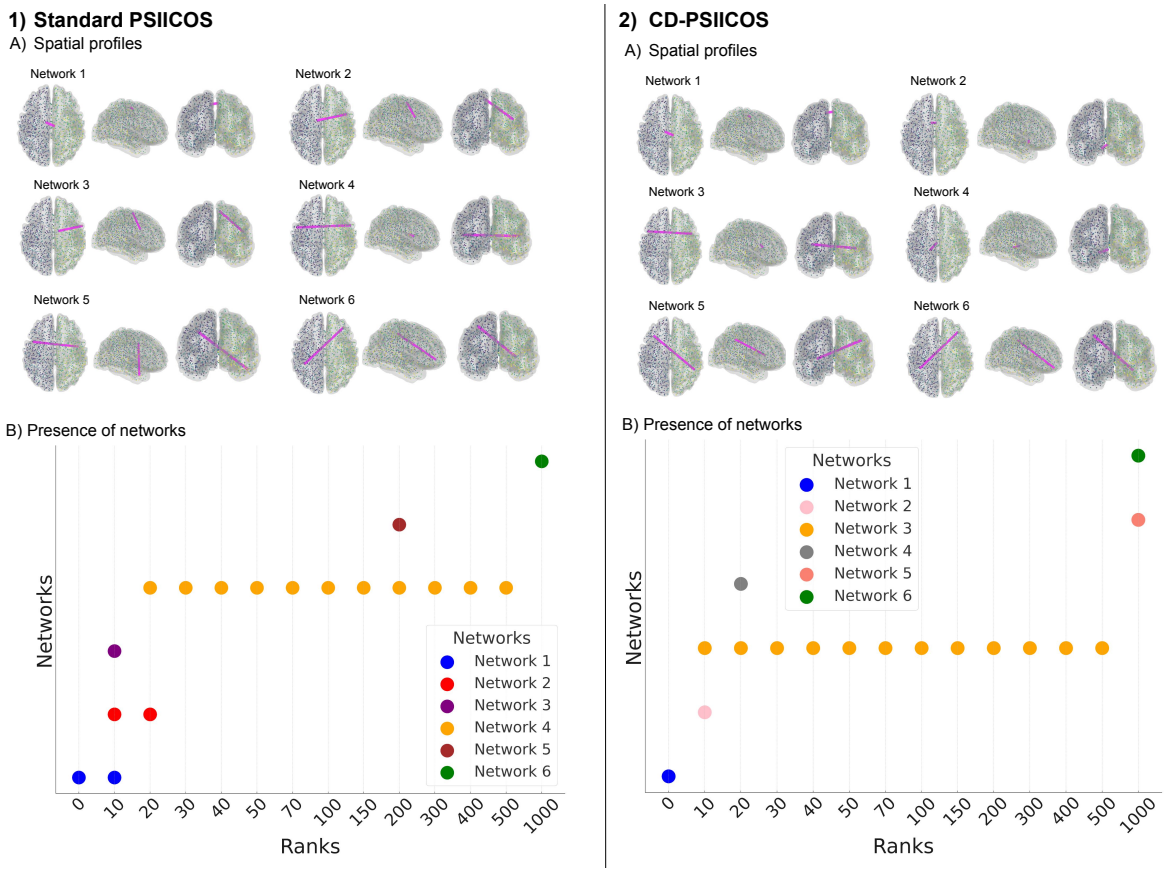

Figure 14: The presence of the networks in the obtained solutions in theta band depending on the type of projector and the projection rank. The blue, orange and green colors indicate the common networks observed in both solutions

The alpha band exhibited stimulus-induced suppression of coupling (see Fig. 15), although the normalization of cross-spectrum revealed the increase of coupling after the stimulus onset. The solution without projection, along with the standard solution at low projection ranks, showed a bias towards the parietal hub. However, as the rank increased and the CD-PSIICOS projector was applied, the focus shifted to the fronto-parietal network (see Fig. 16).

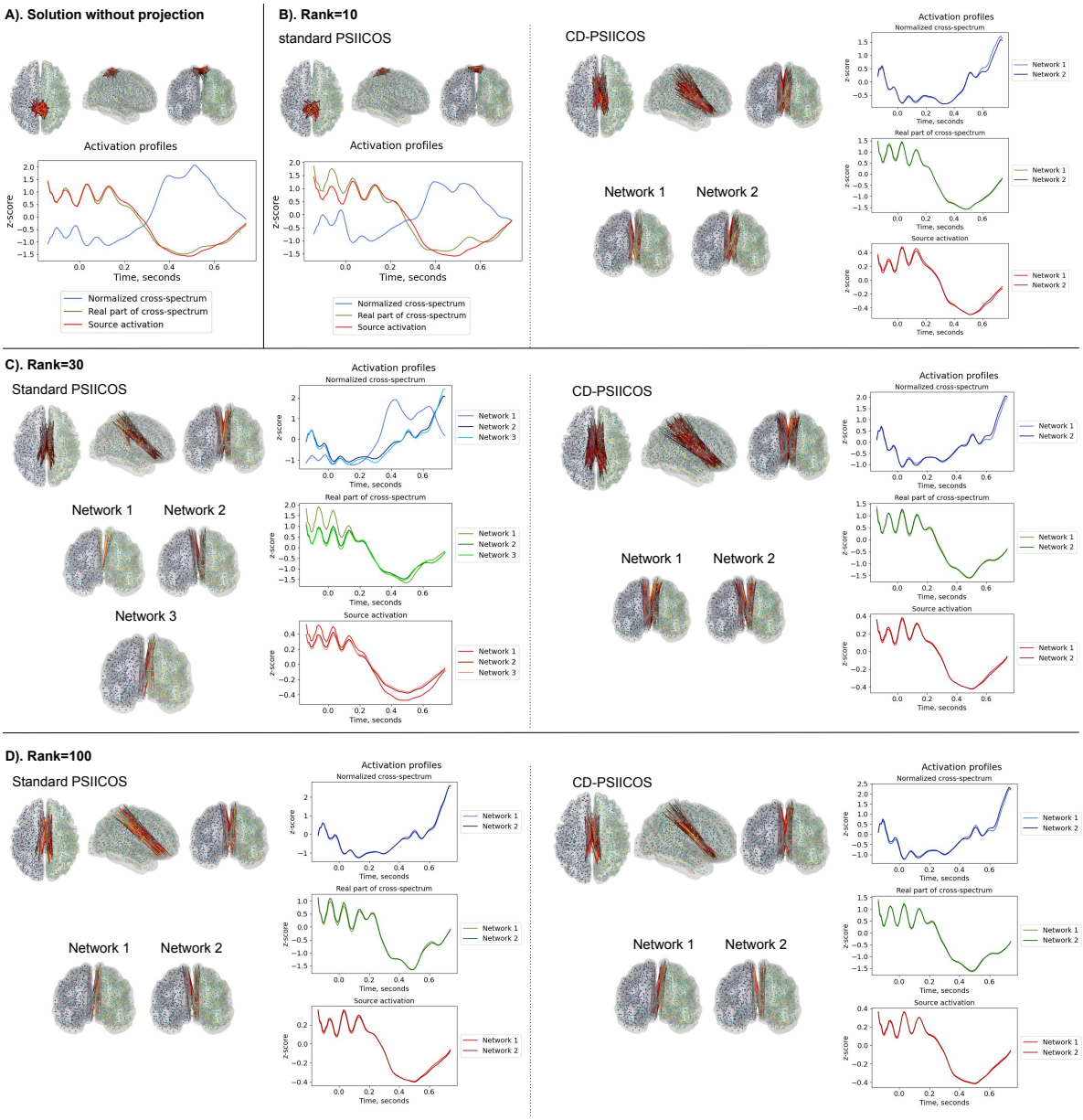

Figure 15: Spatial and activation profiles of the networks in alpha band reconstructed without PSIICOS approach (A) and with standard PSIICOS and CD-PSIICOS approaches at ranks equal to 10 (B), 30 (C), and 100 (D)

For the alpha band, these fronto-parietal networks were identified using the standard PSIICOS approach starting at a projection rank of 30 (Networks 4, 5, Fig. 16, 1.A). In contrast, the CD-PSIICOS solution revealed these networks much earlier, at a projection rank of 10 (Networks 2, 3, Fig. 16, 2.A), demonstrating its ability to suppress spatial leakage more effectively. Notably, the CD-PSIICOS reconstruction lacked the contaminating residuals from the parietal hub observed in the standard PSIICOS solution (Network 3, Fig. 16, 1.A).

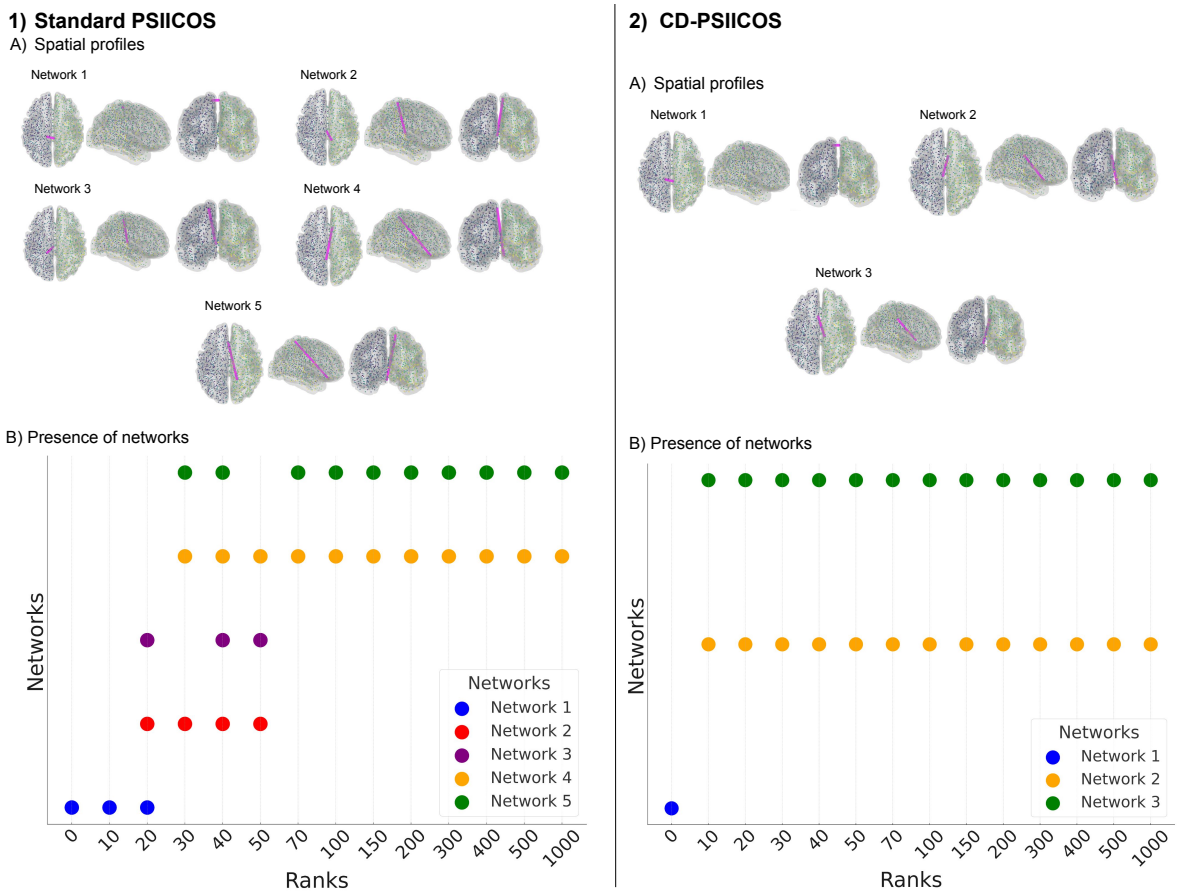

Figure 16: The presence of networks in the obtained solutions in alpha band depending on the type of projector and the projection rank. The blue, orange and green colors indicate the common networks observed in both solutions

In the beta band, the absence of a projector revealed connections in the central hub (see Fig. 17). Interestingly, the standard solution at low projection ranks (up to 20) exhibited a bias towards parieto-temporal connections. However, the CD-PSIICOS solution uncovered deep fronto-parietal connections (see Fig. 17, B). This can be attributed to the fact that power reconstruction in the beta band encompassed a wide range of superficial sources (see Fig.10, C), leading to the suppression of networks involving them. While at lower projection ranks CD-PSIICOS effectively suppressed the widely distributed superficial power-induced networks, the residual spatial leakage was still present at these ranks, indicating that while CD-PSIICOS mitigates the impact of the power-related spatial leakage earlier than the standard solution, further refinement occurs as the projection rank increases.

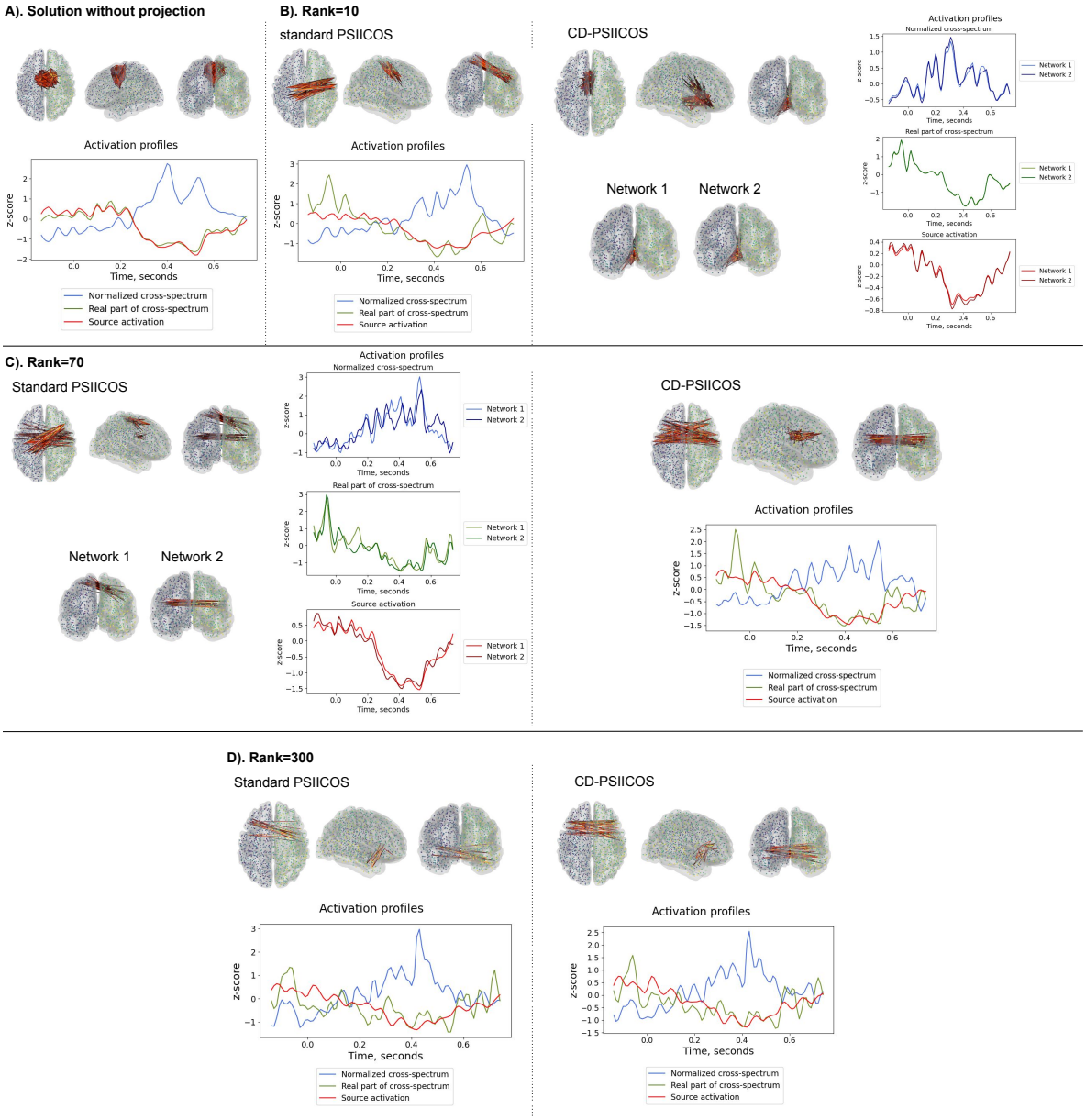

Figure 17: Spatial and activation profiles of the networks in beta band reconstructed without PSIICOS approach (A) and with standard PSIICOS and CD-PSIICOS approaches at ranks equal to 10 (B), 70 (C), and 300 (D)

The analysis of networks at different ranks for the beta band (see Fig. 18) revealed that the most reproducible network involved bilateral fronto-temporal regions (Network 5, see Fig. 18, 1-2.A). This network was identified by the standard PSIICOS solution earlier than by the CD-PSIICOS (rank 30 against rank 70), since CD-PSIICOS was biased towards deep networks, not related to the induced activity (Networks 2-4, 18, 2.A). The power-related network (Network 1, Fig. 18, 1-2.A) was fully suppressed by CD-PSIICOS as early as rank 10, whereas the standard PSIICOS solution achieved similar suppression only starting from rank 20.

Although the standard PSIICOS solution reached the relevant network earlier than CD-PSIICOS in case of beta band, it consistently exhibited additional networks across nearly the entire range of ranks. These included networks resembling the deeper connections to which CD-PSIICOS showed a bias at lower ranks, as well as residual parietal networks (e.g., Network 4, Fig. 18, 1.A). In contrast, once CD-PSIICOS revealed the stable bilateral network, it largely avoided the appearance of extraneous networks. This suggests that CD-PSIICOS more systematically eliminated artifact-driven ¡¡layers¿¿.

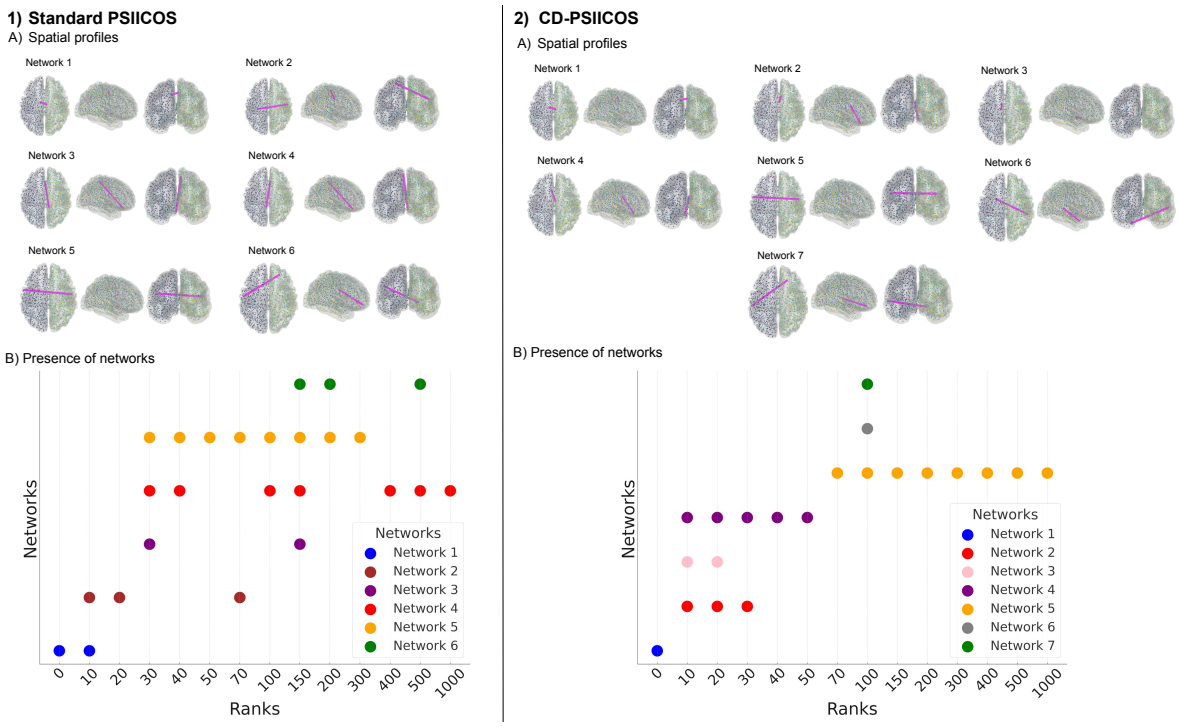

Figure 18: The presence of networks in the obtained solutions in beta band depending on the type of projector and the projection rank. The blue, orange, green, red and purple colors indicate the common networks observed in both solutions

In the gamma band, the solution without projection revealed local frontal connections in the right hemisphere (see Fig.19). As with the other frequency bands, the standard solution at lower ranks remained biased towards these local connections. However, the CD-PSIICOS solution uncovered more distal networks within the frontal regions.

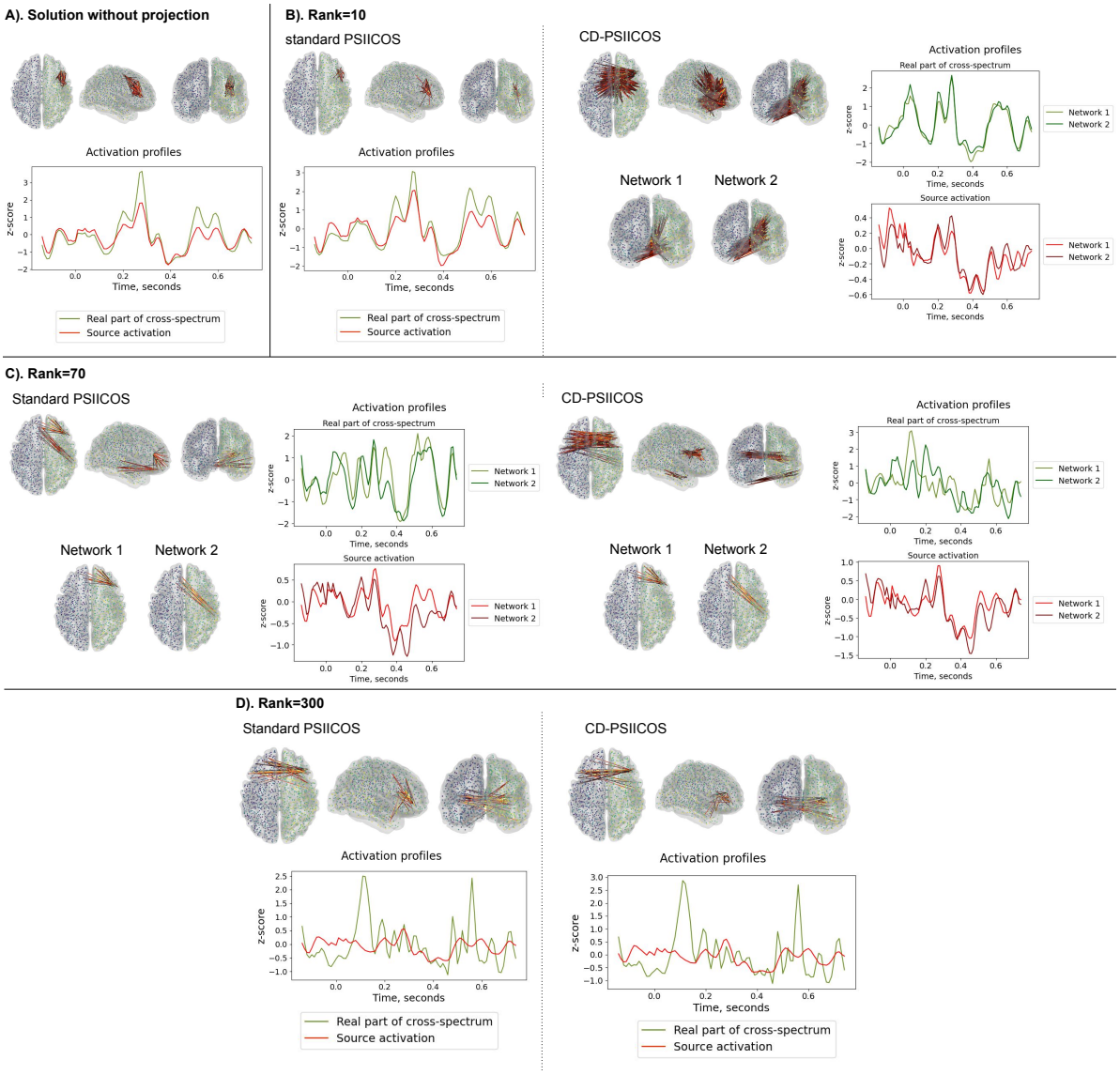

Figure 19: Spatial and activation profiles of the networks in gamma band reconstructed without PSIICOS approach (A) and with standard PSIICOS and CD-PSIICOS approaches at ranks equal to 10 (B), 70 (C), and 300 (D)

The standard PSIICOS solution remained biased towards local power-related connections up to the rank of 70 (see Fig. 20), while CD-PSIICOS fully eliminated these connections much earlier at the rank of 10. Around the rank of 70, both solutions revealed the connections between the right temporal pole and the left frontal and temporal regions (Network 3, Fig. 20, 1.A; Network 4, Fig. 20, 2.A). The presence of this network persisted in CD-PSIICOS solution up to the rank of 300, while in the standard solution it disappeared at the rank of 150 and reappeared at the rank of 1000. However, at rank 1000, the suppression was so strong that not only were the artifacts eliminated, but the true cross-spectral components of the network were also excessively attenuated, resulting in a loss of meaningful connectivity information.

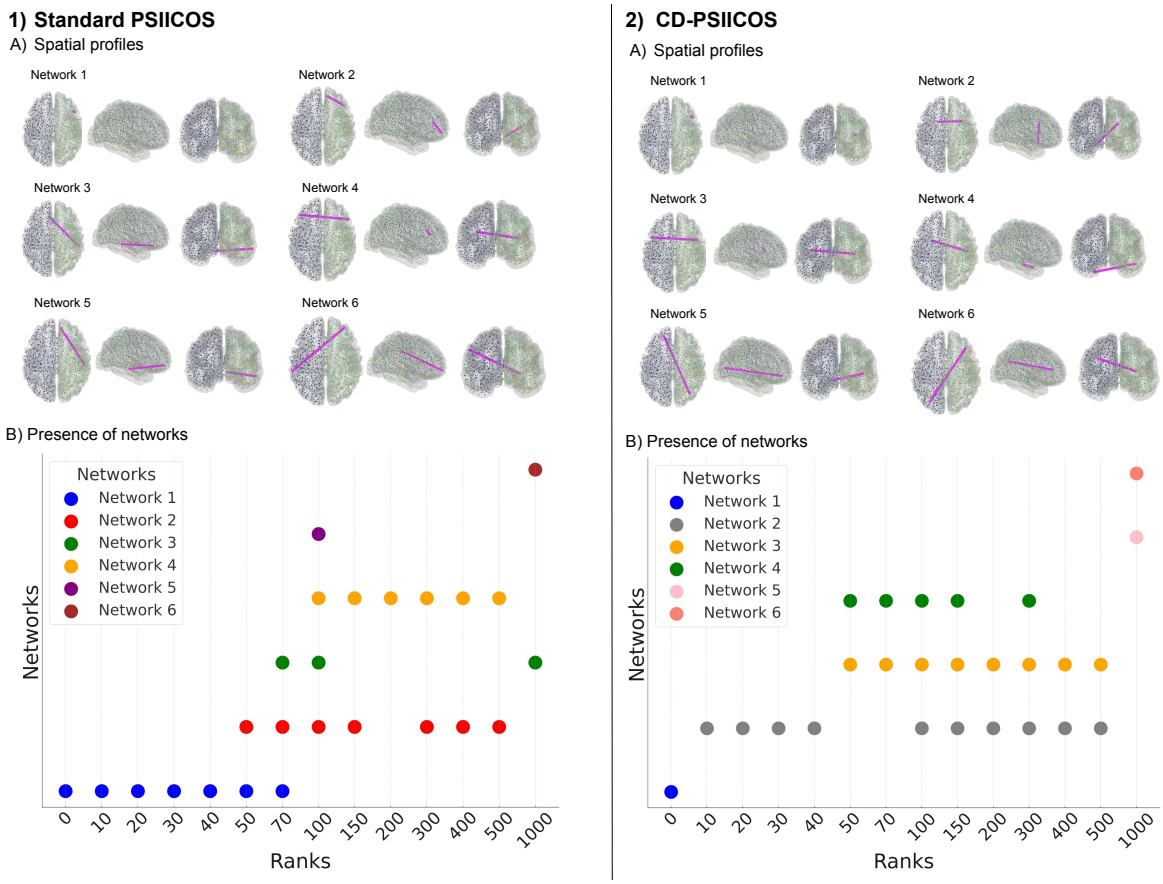

Figure 20: The presence of networks in the obtained solutions in gamma band depending on the type of projector and the projection rank. The blue, orange and green colors indicate the common networks observed in both solutions

The results from the real data demonstrate the improvement of SL suppression obtained by the means of CD-PSIICOS particularly evident in the early suppression of spurious connections and the consistent reconstruction of stable network profiles across ranks. These findings highlight the robustness and reliability of CD-PSIICOS in isolating true functional connectivity, paving the way for more accurate and interpretable network analyses.

4. Discussion

The findings from our study on the Context-Dependent PSIICOS (CD-PSIICOS) framework provide the insights into the advancements in functional connectivity estimation, particularly in accounting for task-related power leakage.

Through a series of realistic simulations, we have shown that CD-PSIICOS outperforms the standard PSIICOS approach, especially at lower projector ranks. The CD-PSIICOS approach also demonstrates robustness across various inverse solutions, including MNE, sLORETA, and DICS, with MNE-derived weighting showing a slight advantage.

The data-driven attenuation curves reveal that the optimal projector rank for CD-PSIICOS is significantly lower than that for the standard PSIICOS, suggesting a more efficient and selective suppression of spatial leakage while retaining true interactions.

The robustness of the CD-PSIICOS solution with respect to the regularization parameter further emphasizes its practical applicability. Unlike many connectivity estimation methods that require careful fine-tuning of regularization to achieve optimal performance, CD-PSIICOS demonstrated consistent results across a wide range of regularization values. This stability is crucial for real-world applications, where experimental conditions and noise levels may vary significantly. These findings align with those of Hincapié et al. (2016), who highlighted the importance of tailoring regularization to the specific goals of analysis, such as power or connectivity estimation.

The validation using real MEG data from the nine participants further supports the efficacy of CD-PSIICOS. The results are consistent with the involvement of theta oscillations in auditory discrimination accompanying mismatch negativity (Ko et al., 2012). Theta coherence observed in the network involving lateral prefrontal regions in both hemispheres indicates the processes of goal-directed actions with cognitive control (Christian et al., 2023) and sustained attention.

The revealed coupling in fronto-parietal networks for alpha band may reflect the suppression of irrelevant information as a part of cognitive control (Palva and Palva, 2011), which is critical during tasks like the oddball paradigms.

Bilateral prefrontal networks detected for beta band may be associated with top-down control, involving decision-making (Alavash et al., 2017), and modulated by dopamine, as evident from the previous research (Chikermane et al., 2024). It is important to note that previous research (Alavash et al., 2017) shows a negative correlation between faster auditory decisions and the power of beta band oscillations, despite the network properties of beta oscillations contributing to quicker decision-making. This suggests that local desynchronization in the beta band may be accompanied by the engagement of long-range networks, which is consistent with the patterns observed in our data.

Finally, gamma frontal networks are associated with cognitive flexibility and processing speed. For example, in decision-making and attention tasks, increased gamma coherence between these areas can reflect improved performance, supporting the integration of sensory inputs and executive functions (ElShafei et al., 2020).

In general, the analysis of real data further underscored the advantages of the CD-PSIICOS approach in reconstructing functional connectivity networks across different frequency bands. CD-PSIICOS consistently revealed relevant networks at lower projection ranks compared to the standard PSIICOS solution, demonstrating its ability to suppress spatial leakage and power-related artifacts earlier in the reconstruction process. In particular, CD-PSIICOS showed greater stability and consistency in network profiles across projection ranks, as evidenced by the persistence of key networks without the appearance of extraneous or spurious connections.

One of the limitations of the presented study is that we did not consider the

behaviour of the proposed method in the following circumstances. Aside from the direct implications of cross-spectral computation, the overestimation of functional connectivity may result from the residual effects of field spread. As highlighted by Schoffelen and Gross (2009), scenarios involving erroneous increases in FC may include amplitude changes in a single neuronal source or both sources, as well as changes in surrounding noise sources that alter the signal-to-noise ratio (SNR). Changes in SNR alone can produce variations in phase locking values that are not associated with a true increase in phase interactions (Muthukumaraswamy and Singh, 2011).

Moreover, there can indeed be genuine amplitude interactions present in the data, which warrant separate research interest. Amplitude coupling is believed to reflect large-scale cortical interactions, showing similarities with previously established fMRI resting-state connectivity patterns (Hipp et al., 2012). The relative independence of amplitude and phase coupling has been reported across various cortical regions and frequencies (Siems and Siegel, 2020; Bruns et al., 2000). A notable distinction between these two coupling modes is that phase coupling pertains to faster oscillations, while amplitude coupling is associated with slower oscillations, typically occurring at frequencies below 0.1 Hz. For instance, infra-slow spontaneous amplitude coupling has recently been reported and hypothesized to be driven by ion concentration dynamics (Krishnan et al., 2018). Another study on MEG signals (Daffertshofer et al., 2018) showed that amplitude coupling was more persistent than phase coupling, although both modes exhibited long-range correlations. Hindriks and Tewarie (2023) demonstrated that non-Gaussian properties, such as co-occurrent high-amplitude bursts captured by co-kurtosis, are crucial for understanding the differences between power correlation and coherence networks. Given the dissociation between phase and power interactions and the fact that genuine phase correlations occur in more specific scenarios, within this paper we focused only on those task-related power interactions that lead to erroneous phase coupling estimates.

Another limitation is that the proposed framework inherently relies on the presence of pronounced oscillatory activity. In scenarios where neural desynchronization occurs– such as the attenuation of alpha or beta rhythms in response to the stimuli – the estimation of cross-spectral changes becomes challenging. Addressing this limitation is crucial for extending the applicability of our method to a broader range of neural phenomena, including those characterized by transient or non-oscillatory activity. One potential direction is to model the disintegration of synchronously active neuronal populations that do not manifest as overt oscillations in the MEG/EEG signals. Recent studies have shown that high-frequency oscillations (HFOs), which originate from small and focal brain regions, can still be detected on the scalp despite their subtle and spatially undersampled nature (Zelmann et al., 2014). However, the standard scalp and grid electrode placements may undersample these focal events. This suggests that even when oscillatory activity is disintegrated or not prominently visible in MEG/EEG recordings, underlying neural interactions may still contribute to measurable signals, if the setup is configured in an optimal way. The suggested modeling can inform the

enhancement of our method with the use of adaptive beamforming, etc.

In conclusion, CD-PSIICOS represents a refinement in functional connectivity analysis by incorporating task-specific contextual information. By incorporating data-driven weights derived from power distributions, the projector effectively focuses on relevant source-space interactions while suppressing spatial leakage and spurious connections. This approach not only enhances the accuracy of connectivity estimates but also contributes a framework for future studies that demand precise differentiation between genuine neural interactions and task-related power modulations.

5. Funding

The article was prepared within the framework of the Basic Research Program at HSE University.

6. Conflict of interest statement

The authors declare that they have no conflicts of interest regarding the publication of this article.

7. Code and data availability

The dataset with the real MEG recordings from the healthy participants (Nugent et al., 2022) can be accessed via OpenNeuro (https://doi.org/10.18112/openneuro.ds004215.v1.0.024).

8. Ethics statement

This study did not record any new dataset neither from animal nor from human subjects. The study used a preexisting MEG dataset recorded from healthy participants and published in (Nugent et al., 2022) along with the necessary ethics statements.

References

Alavash, M., Daube, C., Wöstmann, M., Brandmeyer, A., and Obleser, J. (2017). Large-scale network dynamics of beta-band oscillations underlie auditory perceptual decision-making. *Network Neuroscience*, 1(2):166–191.

Altukhov, D., Kleeva, D., and Ossadtchi, A. (2023). Psiicos projection optimality for EEG and meg based functional coupling detection. *NeuroImage*, 280:120333.

Bassett, D. S. and Bullmore, E. T. (2009). Human brain networks in health and disease. *Current opinion in neurology*, 22(4):340.

Bastos, A. M. and Schoffelen, J.-M. (2016). A tutorial review of functional connectivity analysis methods and their interpretational pitfalls. *Frontiers in systems neuroscience*, 9:175.

Bruns, A., Eckhorn, R., Jokeit, H., and Ebner, A. (2000). Amplitude envelope correlation detects coupling among incoherent brain signals. *Neuroreport*, 11(7):1509–1514.

Chawla, D., Friston, K. J., and Lumer, E. D. (2001). Zero-lag synchronous dynamics in triplets of interconnected cortical areas. *Neural Networks*, 14(6-7):727–735.

Chikermane, M., Weerdmeester, L., Rajamani, N., Köhler, R. M., Merk, T., Vanhoecke, J., Horn, A., and Neumann, W.-J. (2024). Cortical beta oscillations map to shared brain networks modulated by dopamine. *bioRxiv*, pages 2024–02.

Christian, P., Kapetaniou, G. E., and Soutschek, A. (2023). Causal roles of prefrontal and temporo-parietal theta oscillations for inequity aversion. *Social Cognitive and Affective Neuroscience*, 18(1):nsad061.

Daffertshofer, A., Ton, R., Kringelbach, M. L., Woolrich, M., and Deco, G. (2018). Distinct criticality of phase and amplitude dynamics in the resting brain. *Neuroimage*, 180:442–447.

ElShafei, H. A., Fornoni, L., Masson, R., Bertrand, O., and Bidet-Caulet, A. (2020). What's in your gamma? activation of the ventral fronto-parietal attentional network in response to distracting sounds. *Cerebral Cortex*, 30(2):696–707.

Esfahani, Z. G. and Valizadeh, A. (2014). Zero-lag synchronization despite inhomogeneities in a relay system. *PloS one*, 9(12).

Fell, J., Klaver, P., Lehnertz, K., Grunwald, T., Schaller, C., Elger, C. E., and Fernández, G. (2001). Human memory formation is accompanied by rhinal–hippocampal coupling and decoupling. *Nature neuroscience*, 4(12):1259–1264.

Fischer, I., Vicente, R., Buldú, J. M., Peil, M., Mirasso, C. R., Torrent, M., and García-Ojalvo, J. (2006). Zero-lag long-range synchronization via dynamical relaying. *Physical review letters*, 97(12):123902.

Frien, A., Eckhorn, R., Bauer, R., Woelbern, T., and Kehr, H. (1994). Stimulus-specific fast oscillations at zero phase between visual areas v1 and v2 of awake monkey. *Neuroreport*, 5(17):2273–2277.

Fries, P. (2015). Rhythms for cognition: communication through coherence. *Neuron*, 88(1):220–235.

Gollo, L. L., Mirasso, C., Sporns, O., and Breakspear, M. (2014). Mechanisms of zero-lag synchronization in cortical motifs. *PLoS computational biology*, 10(4).

Gray, C. M., König, P., Engel, A. K., and Singer, W. (1989). Oscillatory responses in cat visual cortex exhibit inter-columnar synchronization which reflects global stimulus properties. *Nature*, 338(6213):334–337.

Greicius, M. (2008). Resting-state functional connectivity in neuropsychiatric disorders. *Current opinion in neurology*, 21(4):424–430.

Gross, J., Kujala, J., Hämäläinen, M., Timmermann, L., Schnitzler, A., and Salmelin, R. (2001). Dynamic imaging of coherent sources: studying neural interactions in the human brain. *Proceedings of the National Academy of Sciences*, 98(2):694–699.

Hamalainen, M., Hari, R., Ilmoniemi, R. J., Knuutila, J., and Lounasmaa, O. V. (1993). Magnetoencephalography – theory, instrumentation, and applications to noninvasive studies of the working human brain. *Reviews on modern physics*, 65(2).

Hämäläinen, M. S. and Ilmoniemi, R. J. (1994). Interpreting magnetic fields of the brain: minimum norm estimates. *Medical & biological engineering & computing*, 32:35–42.

Havenith, M. N., Zemmar, A., Yu, S., Baudrexel, S. M., Singer, W., and Nikolić, D. (2009). Measuring sub-millisecond delays in spiking activity with millisecond time-bins. *Neuroscience letters*, 450(3):296–300.

Hincapié, A.-S., Kujala, J., Mattout, J., Daligault, S., Delpuech, C., Mery, D., Cosmelli, D., and Jerbi, K. (2016). Meg connectivity and power detections with minimum norm estimates require different regularization parameters. *Computational intelligence and neuroscience*, 2016(1):3979547.

Hindriks, R. and Tewarie, P. K. (2023). Dissociation between phase and power correlation networks in the human brain is driven by co-occurrent bursts. *Communications biology*, 6(1):286.

Hipp, J. F., Hawellek, D. J., Corbetta, M., Siegel, M., and Engel, A. K. (2012). Large-scale cortical correlation structure of spontaneous oscillatory activity. *Nature neuroscience*, 15(6):884.

Kleeva, D. and Ossadtchi, A. (2021). Detection of instantaneous functional coupling from MEG data by the means of projection in sensor-space cross-spectrum and statistical testing. In *2021 Third International Conference Neurotechnologies and Neurointerfaces (CNN)*, pages 38–41. IEEE.

Ko, D., Kwon, S., Lee, G.-T., Im, C. H., Kim, K. H., and Jung, K.-Y. (2012). Theta oscillation related to the auditory discrimination process in mismatch negativity: oddball versus control paradigm. *Journal of Clinical Neurology*, 8(1):35–42.

König, P., Engel, A. K., Roelfsema, P. R., and Singer, W. (1995). How precise is neuronal synchronization? *Neural Computation*, 7(3):469–485.

Krishnan, G. P., González, O. C., and Bazhenov, M. (2018). Origin of slow spontaneous resting-state neuronal fluctuations in brain networks. *Proceedings of the National Academy of Sciences*, 115(26):6858–6863.

Muthukumaraswamy, S. D. and Singh, K. D. (2011). A cautionary note on the interpretation of phase-locking estimates with concurrent changes in power. *Clinical neurophysiology: official journal of the International Federation of Clinical Neurophysiology*, 122(11):2324–2325.

Nolte, G., Bai, O., Wheaton, L., Mari, Z., Vorbach, S., and Hallett, M. (2004). Identifying true brain interaction from EEG data using the imaginary part of coherency. *Clinical Neurophysiology*, 115(10):2292–2307.

Nolte, G., Ziehe, A., Nikulin, V. V., Schlögl, A., Krämer, N., Brismar, . f. T., and Müller, K.-R. (2008). Robustly estimating the flow direction of information in complex physical systems. *Physical review letters*, 100(23):234101.

Nugent, A. C., Thomas, A. G., Mahoney, M., Gibbons, A., Smith, J. T., Charles, A. J., Shaw, J. S., Stout, J. D., Namyst, A. M., Basavaraj, A., et al. (2022). The NIMH intramural healthy volunteer dataset: A comprehensive MEG, MRI, and behavioral resource. *Scientific Data*, 9(1):518.

Ossadtchi, A., Altukhov, D., and Jerbi, K. (2018). Phase shift invariant imaging of coherent sources (psiicos) from meg data. *NeuroImage*, 183:950–971.

Palva, S. and Palva, J. M. (2011). Functional roles of alpha-band phase synchronization in local and large-scale cortical networks. *Frontiers in psychology*, 2:204.

Pascual-Marqui, R. D. et al. (2002). Standardized low-resolution brain electromagnetic tomography (sloreta): technical details. *Methods Find Exp Clin Pharmacol*, 24(Suppl D):5–12.

Rajagovindan, R. and Ding, M. (2008). Decomposing neural synchrony: toward an explanation for near-zero phase-lag in cortical oscillatory networks. *Plos one*, 3(11).

Rodriguez, E., George, N., Lachaux, J.-P., Martinerie, J., Renault, B., and Varela, F. J. (1999). Perception's shadow: long-distance synchronization of human brain activity. *Nature*, 397(6718):430–433.

Roelfsema, P. R., Engel, A. K., König, P., and Singer, W. (1997). Visuomotor integration is associated with zero time-lag synchronization among cortical areas. *Nature*, 385(6612):157–161.

Schoffelen, J.-M. and Gross, J. (2009). Source connectivity analysis with meg and EEG. *Human brain mapping*, 30(6):1857–1865.

Siems, M. and Siegel, M. (2020). Dissociated neuronal phase-and amplitude-coupling patterns in the human brain. *NeuroImage*, page 116538.

Stam, C. J., Nolte, G., and Daffertshofer, A. (2007). Phase lag index: assessment of functional connectivity from multi channel EEG and MEG with diminished bias from common sources. *Human brain mapping*, 28(11):1178–1193.

Vicente, R., Gollo, L. L., Mirasso, C. R., Fischer, I., and Pipa, G. (2008). Dynamical relaying can yield zero time lag neuronal synchrony despite long conduction delays. *Proceedings of the National Academy of Sciences*, 105(44):17157–17162.

Zelmann, R., Lina, J.-M., Schulze-Bonhage, A., Gotman, J., and Jacobs, J. (2014). Scalp EEG is not a blur: it can see high frequency oscillations although their generators are small. *Brain topography*, 27:683–704.